AD-A155 405 HETERODYNE HOLOGRAPHIC INTERFEROMETRY FOR VISUALIZATION 1/2
OF SURFACE ACOUSTIC WAVES(U) JOHNS HOPKINS UNIV
BALTIMORE MD DEPT OF MATERIALS SCIENCE AND..
UNCLASSIFIED J W WAGNER NOV 84 ONR-85-1 N00014-82-K-0741 F/G 14/5 NL

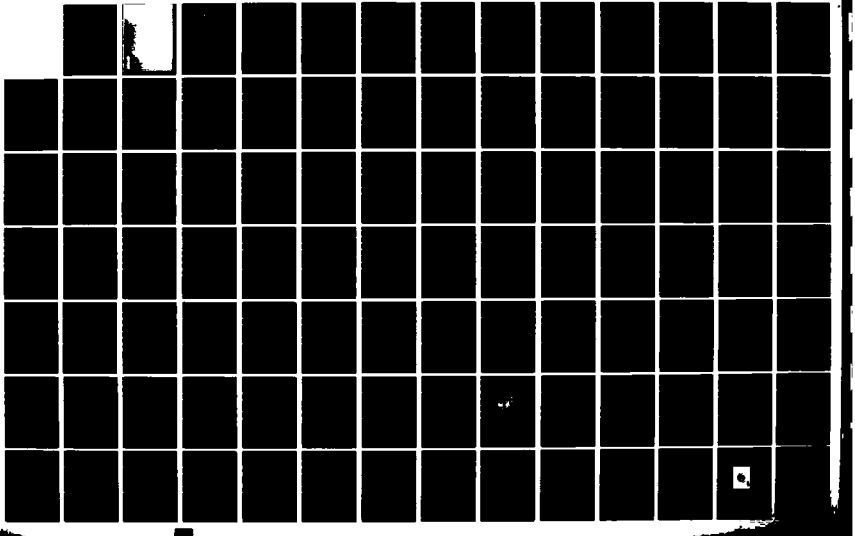

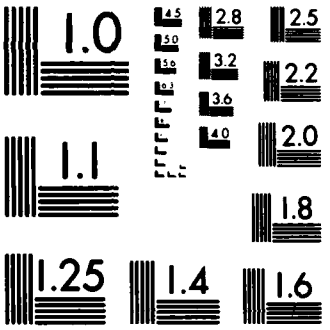

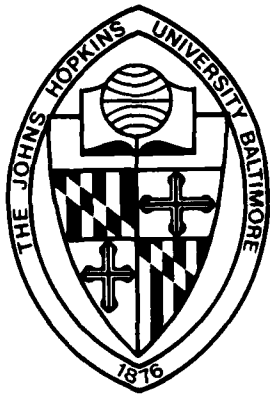

HETERODYNE HOLOGRAPHIC INTERFEROMETRY FOR VISUALIZATION OF SURFACE ACOUSTIC WAVES

James W. Wagner
Materials Science and Engineering Department
The Johns Hopkins University
Baltimore, MD 21218

TECHNICAL REPORT
ONR-TECH-85-1

Office of Naval Research
Contract N00014-82-K-0741

FULL FIELD VISUALIZATION OF SURFACE ACOUSTIC WAVES
November 1984

UNCLASSIFIED

SECURITY CLASSIFICATION OF THIS PAGE (When Data Entered)

REPORT DOCUMENTATION PAGE		READ INSTRUCTIONS BEFORE COMPLETING FORM
1. REPORT NUMBER ONR-TECH-85 -1	2. GOVT ACCESSION NO.	3. RECIPIENT'S CATALOG NUMBER
4. TITLE (and Subtitle) Heterodyne Holographic Interferometry for Visualization of Surface Acoustic Waves		5. TYPE OF REPORT & PERIOD COVERED Interim 6. PERFORMING ORG. REPORT NUMBER
7. AUTHOR(s) James W. Wagner		8. CONTRACT OR GRANT NUMBER(s) N00014-82-K-0741
9. PERFORMING ORGANIZATION NAME AND ADDRESS Materials Science and Engineering Dept. 102 Maryland Hall The Johns Hopkins University; Balto., MD 21218		10. PROGRAM ELEMENT, PROJECT, TASK AREA & WORK UNIT NUMBERS NR 384-813 RR 011-08-01
11. CONTROLLING OFFICE NAME AND ADDRESS O N R Code 412 Dept. of Navy Arlington, VA 22217		12. REPORT DATE November, 1984 13. NUMBER OF PAGES 110
14. MONITORING AGENCY NAME & ADDRESS(if different from Controlling Office)		15. SECURITY CLASS. (of this report) Unclassified 15a. DECLASSIFICATION/DOWNGRADING SCHEDULE

16. DISTRIBUTION STATEMENT (of this Report)

Approved for public release, distribution unlimited

17. DISTRIBUTION STATEMENT (of the abstract entered in Block 20, if different from Report)

Approved for public release, distribution unlimited

18. SUPPLEMENTARY NOTES

19. KEY WORDS (Continue on reverse side if necessary and identify by block number)

Holography
Holographic Inteferometry
Heterodyne Holography
Surface Waves
Nondestructive Evaluation

20. ABSTRACT (Continue on reverse side if necessary and identify by block number)

A technique for recording and visualizing acoustic wavefronts over a finite field of view and with a resolution on the order of Angstroms has been developed. Multiple exposure holograms of an aluminum test block were used to record the

DD FORM 1 JAN 73 1473 EDITION OF 1 NOV 65 IS OBSOLETE
S/N 0102-LF-014-6601

UNCLASSIFIED
SECURITY CLASSIFICATION OF THIS PAGE (When Data Entered)

surface displacements resulting from the detonation of a small explosive charge placed on the object surface. The primary wavefronts resulting from the explosive charge were sufficiently large as to be visible upon reconstruction of the holographic interferograms. In addition, details of the surface wavefronts which could not be deduced using conventional holographic interferometry were measured and displayed by modifying the pulsed recording geometry and subsequently applying heterodyne interferometric analysis to the holograms to interpolate between the observed interferometric fringes. Although theory predicts that still greater resolution is possible, fringe interpolation to 1/900 of a fringe (about 3A displacement) was demonstrated. Based on these experimental results and the mathematical relationships which have been developed to describe system performance, it appears likely that a practical system for studying sub-Angstrom transient phenomena may be realized using heterodyne holographic interferometry.

Abstract

A technique for recording and visualizing acoustic wavefronts over a finite field of view and with a resolution on the order of Angstroms has been developed. Multiple exposure holograms of an aluminum test block were used to record the surface displacements resulting from the detonation of a small explosive charge placed on the object surface. The primary wavefronts resulting from the explosive charge were sufficiently large as to be visible upon reconstruction of the holographic interferograms. In addition, details of the surface wavefronts which could not be deduced using conventional holographic interferometry were measured and displayed by modifying the pulsed recording geometry and subsequently applying heterodyne interferometric analysis to the holograms to interpolate between the observed interferometric fringes. Although theory predicts that still greater resolution is possible, fringe interpolation to 1/900 of a fringe (about 3Å displacement) was demonstrated. Based on these experimental results and the mathematical relationships which have been developed to describe system performance, it appears likely that a practical system for studying sub-Angstrom transient phenomena may be realized using heterodyne holographic interferometry.

A-1

Table of Contents

INTRODUCTION

To date, conventional techniques for measuring and studying transient surface wave phenonena have been limited to transducer techniques which provide a time record of surface displacement at a single position on an object surface. Piezoelectric, capacitive, magnetic, and single point interferometric techniques all fall into this category. For many testing and measurement applications, these techniques are quite adequate. However, some studies are difficult if not impossible to perform with such transducer systems. If one wishes to investigate the interaction of surface waves with a surface defect, for example, a single point transducer must be moved around the defect area and the experiment repeated for each new transducer location in order to map out changes in the amplitude and shape of the surface wavefront as it is diffracted and attenuated by the defect. For some transducer types the effects of mounting the transducer on the surface must also be taken into account. Further, the acoustic wave source must be very reproducible so that one is assured that for each new placement of the transducer, the wave which is propagated is identical to the one before it. Alternatively, one can imagine an experi-

ment where an array of noncontacting transducers are positioned on an object surface so that surface displacement over a fixed field may be recorded as a function of time and position for a single acoustic event. The cost of implementing such a system and restrictions on object surface geometry would seem to preclude the use of such a system as a practical measurement technique.

Holographic techniques, on the other hand, provide a means to interferometrically compare changes in surface topography of objects of arbitrary shape over a finite field of view. Time-averaged holographic interferometry has been used to study the rather large surface displacements associated with mechanical resonances. Transient surface displacements associated with impact testing and high energy ultrasonic testing have been recorded using double exposure pulsed holography. In both of these holographic techniques, interferometric fringes are observed in the reconstructed holographic image wherever the surface is displaced by an amount greater than one half the wavelength of the illuminating laser light. Thus displacements less than about 250nm (2500A) do not give rise to holographic fringes. Consequently sub-fringe wavefronts or sub-fringe detail of large wavefronts cannot be discerned by either of these holographic techniques. However, by modifying the holographic recording geometry and applying heterodyne analysis techniques to the recorded hologram, full field measurement and visualization of sub-fringe surface displacements such as those associated with traveling surface acoustic wave may be achieved.

Full field recording is achieved using pulsed holography to "freeze" surface motion at a particular instant in time. Using double exposure holography, the surface

topography of a test specimen at different instants in time may be interferometrically compared. The double exposure hologram records two virtual images of the test specimen which, when reconstructed by reillumination of the hologram with its reference beam, appear in space at the original object location relative to the hologram plate. These two virtual images may be used as virtual objects for an interferometer if reimaged on an observation plane. The interference pattern produced at the observation plane is identical to that which would be observed if the light reflecting from the surfaces of two nearly identical real objects were combined by substituting the object surfaces for the mirrors of a Michelson interferometer.

This Michelson interferometer analogy for holographic interferometry proves to be useful in predicting the effects of surface displacements on the observed holographic interference pattern. In fact the results obtained using this analogy are exact for the case where both the viewing angle and the angle of object illumination are normal to the object surface when the hologram is exposed and where plane wave illumination is used. Assuming then that this is indeed the case one can see that local changes in surface displacement alter the optical pathlength from the object surface to the point of observation. If at a single point on the object there is no displacement between the first and second holographic exposures, then the light reflecting from corresponding points of the two virtual objects travels exactly the same distance to the observation plane. Consequently, the electric fields of the two reflected rays will be in phase and interfere constructively to give a bright point in the observation plane. If, on the other hand, at a different point on the object, some displacement occurred between exposures, then the light reflecting from corresponding points on the two virtual objects will not be in phase

at the observation plane. If the displacement which occurred between exposures was sufficient to cause an optical pathlength change of one half the wavelength of the illuminating light, then the two rays from the corresponding points on the virtual object will differ in phase by 180° thus interferring destructively giving a dark point in the observation plane. As in the case of a Michelson interferometer, a object motion of one-half wavelength yields one whole wavelength of optical pathlength change. Therefore the interferometric fringes formed over the image of the object in the observation plane appear to map out contours of constant displacement where the contour interval is one half the wavelength of the illuminating light.

With the establishment of this half wavelength contour, or fringe, interval the sensitivity limit of visually interpreted holographic interferograms is set. In the experiment reported in this work, an argon ion laser with an output wavelength of 514.5nm was used. Thus one full fringe corresponds to a surface displacement of 257.3nm. One can readily discern one-half a fringe and therefore may resolve down to 128.6nm by simply counting fringes observed in the output plane of the holographic interferometer. Unfortunately surface displacement amplitudes generated by conventional ultrasonic transducers may range from 0.01nm to tens of nanometers and are, therefore, well below the limit of resolution for visually interpreted holographic interferometry. In other words, if a flat mirror were used as a test object and a hologram was exposed before and during excitation of the mirrored object by a conventional ultrasonic transducer, no fringes would be observed in the observation plane of the holographic interferometer.

Sub-fringe displacement information, however, is recorded by the hologram and may be extracted using heterodyne interferometric techniques to read out the holographic record. Heterodyne techniques employ any of several methods to ensure that light arriving at the output plane from one virtual object is at a slightly different frequency from the light arriving from the other virtual object. The effect of frequency shifting one of the light beams is to cause the intensity of the image in the output plane to vary periodically at the difference frequency of the two beams. While the frequency of the intensity variation is the same at every point on the object surface, different points in the image plane may not fluctuate precisely in phase with each other. The degree of phase difference in intensity fluctuation between two points in the observation plane is directly related to the difference in surface displacement between the two points. Thus if a one-half fringe difference were observed between two points using conventional holographic interferometry, there would be a 180° phase difference in intensity fluctuation measured between the same two points in the heterodyne case. Since one fringe corresponds to a 360° phase difference, then each degree of phase difference corresponds to an object displacement of 257.3nm x 1/360 or about 0.7nm for the 514.5nm line of the argon ion laser. Note that sensitivities in this range should permit detection of displacements from conventional ultrasonic sources. The ability to resolve much smaller displacements is limited by factors which may be optimized for a particular application. These factors include quantum noise at the detectors, speckle noise in the image, and environmental effects.

Consideration must also be given to the process of holographically recording a traveling acoustic wavefront. For the studies reported in this work, a pulsed Nd:YAG laser with a frequency doubled output at 532nm was used. The laser had a fixed pulse duration of 9ns and a peak output energy per pulse of about 600mJ. The diffraction efficiency of holograms recorded of objects in motion is a function of the velocity of the displacements along the direction of the bisector of the illumination and viewing angles. For periodic displacements, this velocity is determined by the product of the frequency and amplitude of the surface waves. For the amplitude and frequency spectrum of the surface waves studied during this investigation, the 9ns laser pulse duration was sufficiently short to ensure only a 0.5% reduction in holographic diffraction efficiency. Thus holographic reconstruction efficiency is not significantly degraded by small acoustic perturbations of the object surface. Likewise, the accuracy with which such small perturbations are recorded was shown to remain sufficiently high to permit accurate surface displacement measurements to the sub-Angstrom level.

BACKGROUND

The advantages of using pulsed holography and heterodyne analysis for studying traveling surface acoustic waves become apparent once the operating principles are well understood. To obtain such an understanding it is useful to review the principles of classical interferometry and holography. This section includes a discussion of interferometry as a tool for measuring dynamic surface displacement. The Michelson interferometer is used as an example with special attention paid to noise sources which limit displacement sensitivity and are to some degree common to the heterodyne holographic system. These noise sources include pathlength instabilities, detector shot noise, and thermal noise in amplifiers. Heterodyne interferometry, the nature of heterodyne signals, and its effect on overall signal to noise ratio is discussed.

Holography relieves the restrictions imposed by classical interferometry on the types of test objects that may be analyzed. Typically one may inspect flatness of mirrors or symmetry of convex or concave optical surfaces using classical interferometers. Using holography, however, one may inspect more complex and even diffuse surfaces. A hologram may be used to reconstruct any arbitrary reference wavefront especially that reflected by the test object at some earlier point in time. This reference wavefront may then be combined with the object wavefront to produce an interference pattern over the image of the object indicative of surface displacements which may have occurred subsequent to the initial holographic expo-

sure. Thus, the entire object within the field of view of the holographic interferometer may be holographically recorded and interferometrically compared. The principles of holographic wavefront reconstruction, the use of pulsed recording techniques for freezing rapidly occurring displacements, and the application of heterodyne techniques to improve holographic sensitivity will be discussed.

Interferometry

The Michelson interferometer shown schematically in Figure 1 will be used to illustrate the interferometric principles applied to surface displacement measurements. In every case it will be assumed that coherent, single mode, polarized laser illumination is used. The laser beam entering the interferometer from the left is split by partial reflectance into two beams at the beamsplitter. The portion of the beam deflected upwards in the figure is reflected by the reference mirror back through the beamsplitter and onto a photodetector. That portion of the laser beam not initially deflected by the beamsplitter is reflected from the test object surface and returned to the splitter where it is combined with the reference beam and deflected onto the photodetector.

The object and reference waves arriving at the detector may be expressed by their respective analytic signal representations (Yariv, 1976) which is the harmonic solution to the free space optical wave equation for the electric field at the detector

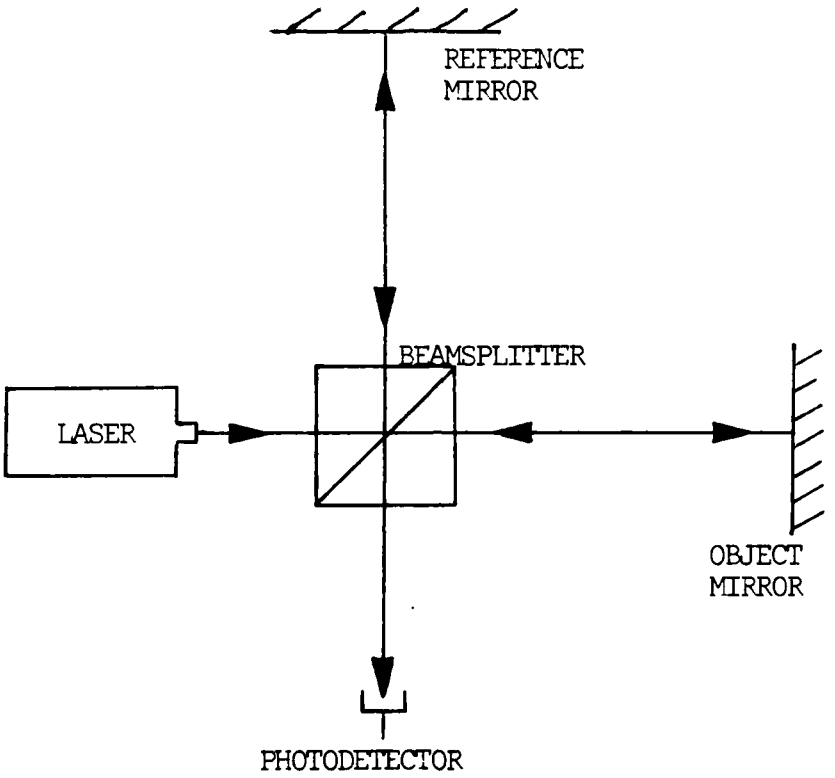

Figure 1: Michelson Interferometer

location:

$$U_R = A_R e^{j\omega t} \qquad (1)$$
$$U_O = A_O e^{j(\omega t + kdl)}$$

where

U_R = reference beam

U_O = object beam

A_R = field amplitude of reference beam

A_O = field amplitude of object beam

ω = radian frequency of the laser

t = time

k = propagation constant $2\pi/\lambda$

dl = total pathlength difference between the reference and object beams.

These expressions represent the amplitudes of the two optical beams. Photodetectors, however are square-law devices sensitive to radiant intensity not amplitude. Therefore the electrical signal generated by the detector will be proportional to the light intensity incident on the detector.

$$I_D = |U_O + U_R|^2 \qquad (2)$$
$$= (U_O + U_R)(U_O^* + U_R^*)$$

where

U_O^* = complex conjugate of U_O

U_R^* = complex conjugate of U_R.

Thus,

$$I_D = A_O^2 + A_R^2 + A_O A_R [e^{jkdl} + e^{-jkdl}]$$
$$= A_O^2 + A_R^2 + 2A_O A_R \cos kdl$$
$$= 1 + 2\frac{A_O A_R}{A_O^2 + A_R^2} \cos kdl.$$

If $A_O = A_R$, then

$$I_D = 2A^2(1 + \cos kdl). \quad (3)$$

Since in both legs of the interferometer, the beam is folded back on itself, the pathlength difference,dl, resulting from a normal surface displacement, D, is twice the displacement amount. Equation 3 may now be rewritten:

$$I_D = 2A^2(1 + \cos 2kD)$$
$$= 2A^2(1 + \cos(\frac{4\pi}{\lambda}D)) \quad (4)$$

It can be seen then that minima in the light intensity falling on the detector occur when $D = n\frac{\lambda}{4}$, n = 1,2,3...

Although the Michelson interferometer in this basic form has been used to

detect acoustic signals (Wellman, 1980), several modifications may be made to improve its performance. By twice differentiating Equation 4 with respect to D one observes that the greatest change in intensity for a given surface deflection less than $\lambda/2$ occurs when $D = (2n+1)\lambda/8$. One approach, then, to obtaining maximum sensitivity to surface displacements is to actively stabilize the optical path difference between the object and reference legs using an electro-mechanical feedback arrangement to drive the reference mirror. An additional benefit realized by using an electronmechanical feedback system is that the surface displacement signals of interest appear as either control or error signals which may be easily picked off of the feedback control circuit. The mirror drive control signal follows and may therefore be used as a measure of low frequency surface displacements (Leiner, 1978). The feedback error signal, on the other hand, tracks pathlength variations resulting from acoustic waves, for example, which occur at frequencies beyond the response limit of the feedback system (Palmer, 1977; Palmer, 1979; Smeets, 1977; Emmony, 1982). Techniques other than feedback stabilization have been used to ensure peak sensitivity of the interferometer. In one system developed at RCA labs (Mezrich, 1974) the reference mirror is moved at a low frequency and relatively large amplitude to assure that at some point in the measurement period the interferometer is in its optimum configuration. This technique works espesially well for measuring continuous, periodic signals. In such cases the largest signal recorded during the test interval corresponds to the point of maximum sensitivity and is retained for analysis. Another technique introduces a 90° phase shift between orthogonal polarizations of the reference beam. When the object beam is interfered with each of the reference components, the two resulting interference intensity signals may be squared and then added thus linearizing the interferometer

at its peak sensitivity (Vilkomerson, 1976; Peck, 1953). Finally, optical heterodyne techniques may be used to minimize sensitivity variations caused by pathlength instabilities. This technique will be reviewed in some detail in following sections.

It is usually assumed that in the case of the Michelson interferometer the shot noise of the photodetector sets the fundamental limit to the interferometer's sensitivity (Kwaaitaal, 1980). This may not always be the case, however. Other contributions to the total noise of the interferometer system include laser noise, environmental (mechanical) noise, and electronic noise. Kwaaitaal's work indicates that laser noise can be made insignificant if a single mode laser is used and the frequency content of the detected signal is above 10kHz (Kwaaitaal, 1980). Electronic and environmental noise, however, are not so easily neglected.

Consider first the noise associated with a photodetector/amplifier combination required to obtain a voltage signal analog to the light intensity incident on the detector. Two general classes of photodetectors will be considered - photoemissive and solid state. Specific representatives of these two classes are the photomultiplier tube and the junction photodiode, respectively. In both cases light incident on the active regions of these devices (i.e. photocathode or depletion region) liberates electrons or generates electron-hole pairs which contribute to current flow through the device. This signal current may be described as follows:

$$I_S = \frac{\eta q P}{h \nu} \tag{5}$$

where

η = quantum efficiency in carriers/photon

q = electron charge

P = incident light intensity

h = Plank's constant

ν = light frequency.

Owing to the quantum nature of light there is an associated shot noise with a spectral density function

$$S(\nu)=2\bar{N}q^2, \tag{6}$$

where $\bar{N}$ represents the average carrier emission rate (Yariv, 1976). Since the average current, $\bar{I}$, is $q\bar{N}$, the shot noise power for a given frequency bandwidth, B, can be written:

$$\overline{i_N^2}=2q\bar{I}B. \tag{7}$$

Thus if shot noise were the only source of noise in the detector/amplifier system, then the signal to noise ratio could be computed from Equations 5 and 7 as follows:

$$S/N=\frac{i_S^2}{\overline{i_N^2}}=\frac{(\eta qP/h\nu)}{2q(\eta qP/h\nu)B}$$

$$S/N=\frac{\eta P}{2h\nu B}. \tag{8}$$

The quantum efficiency of common photocathode materials is typically about 10% versus about 30% for a silicon photodiode (Anderson and McMurtry, 1966). Thus if one considers that the performance of a detector/amplifier system is shot noise limited, then better signal to noise ratio will be obtained using solid state photodiode detectors.

In a shot noise limited system the minimum detectable surface displacement may be computed for the case of the Michelson interferometer. Equation 4 provides a relation for the power incident on a photodetector for a mirror displacement, D.

$$P=P_0(1+M\cos\frac{4\pi}{\lambda}D),$$

where M (modulation factor) $= 2\frac{A_O A_R}{A_O^2+A_R^2}$

$P_0 = A_O^2+A_R^2$.

In the case where an acoustic wave is launched on the mirror surface, the displacement, D is the sum of a static component and a dynamic component. Using Kwasitaal's notation:

$$D=X+x$$

where X = mirror position

$x = \hat{x}\sin 2\pi ft$.

Thus the power incident on the photodetector is

$$P = P_0(1+M\cos[\frac{4\pi}{\lambda}(X+x)])$$
$$= P_0(1+M\cos(\frac{4\pi}{\lambda}X)\cos(\frac{4\pi}{\lambda}x) - M\sin(\frac{4\pi}{\lambda}X)\sin(\frac{4\pi}{\lambda}x))$$

For $x << \lambda$,

$$P = P_0(1+M\cos(\frac{4\pi}{\lambda}X) - M\frac{4\pi}{\lambda}x\sin(\frac{4\pi}{\lambda}X)). \quad (9)$$

Note that only the third term contains the signal displacement factor, x. Consequently the average photocurrent contributing to detector shot noise derives from the first two terms of Equation 9:

$$i_N^2 = 2q\bar{I}B$$
$$= 2q(\eta q P_0/h\nu)(1+M\cos(\frac{4\pi}{\lambda}X))B.$$

The signal current is

$$i_s = (\frac{\eta q P_0}{h\nu})M(\frac{4\pi}{\lambda})x\sin(\frac{4\pi}{\lambda}X).$$

The signal to noise ratio is now computed as

$$SNR = \frac{i_s^2}{i_N^2} = \frac{\eta P_0}{2h\nu B}(\frac{4\pi}{\lambda}x)^2\frac{M^2\sin^2\frac{4\pi}{\lambda}X}{1+M\cos\frac{4\pi}{\lambda}X}. \quad (10)$$

For other than ideal systems, $M<1$ causing the maximum signal to noise to occur for $X \approx 3\lambda/16$. This result is shown graphically in Figure 2a. Note that , somewhat surprisingly, the best signal to noise ratio is not obtained when $x=\lambda/8$, i.e. where the slope of the signal curve is greatest (Figure 2b). Instead the best SNR is obtained for $X \approx 3\lambda/16$. One can reconcile this result by observing that the $3\lambda/16$ point represents a compromise between maximum signal gain and minimum shot noise. The background light level at the point of maximum signal slope ($X=\lambda/8$) is greater than at the computed SNR maximum. Therefore the average photodetector current and consequently the shot noise will be greater at this point. On the other hand, when $X=\lambda/4$, the shot noise is at a minimum. Unfortunately the signal gain is at a minimum as well. Therefore the optimum value for X must lie somewhere between $\lambda/8$ and $\lambda/4$. Using the argon ion laser line at 514.5nm, and a 0.5mm diameter silicon detector, and 0.05mW/cm ^{2} output field intensity typical of a holographic interferometry system, the minimum dynamic displacement sensitivity for a SNR=1 can be computed using Equation 10. For $X=3\lambda/16$, $M=0.9$, and a 1Hz bandwidth,

$$x=4.71\times10^{-8}m.$$

Note that this is about 500Å and is, therefore, far less sensitive than desirable. Fortunately, sensitivity may be improved by increasing laser illumination, hologram efficiency, detector area, and by using heterodyne detection all of which tend to increase the light intensity incident on the photodetector. Bear in mind that this rather disappointingly poor sensitivity is largely the result of the low light intensity

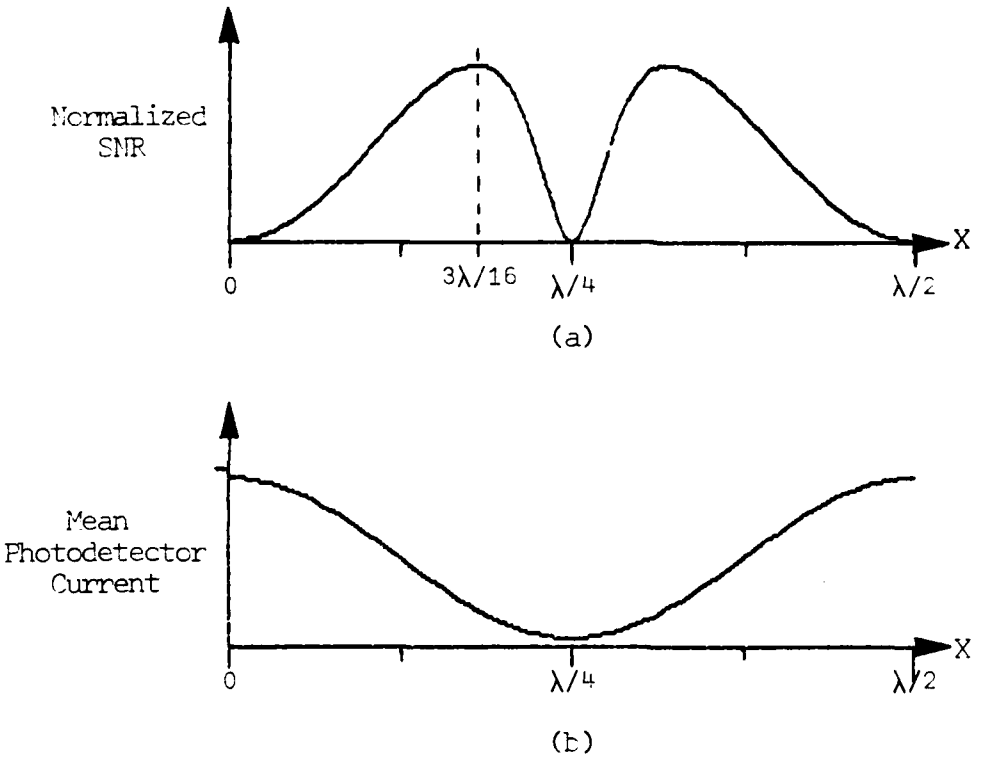

Figure 2: a) Signal to Noise Ratio and b) Photocurrent as a function of pathlength difference, X, in a Michelson interferometer.

figure which was selected to represent actual intensities encountered in holographic interferometry.

Heterodyne Interferometry

Heterodyne interferometry provides another alternative to path stabilization for immunity to environmental noise sources. In addition, the application of heterodyne techniques to holographic interferometry allows for interpolation between fringes to obtain sensitivity to static displacements comparable to real time dynamic detection sensitivities obtained by classical interferometers. The basic difference between heterodyne and homodyne interferometry is that the two wave fronts to be interfered in the output plane of the interferometer are shifted in frequency relative to each other for heterodyne and not for homodyne. The light intensity incident on the photodetector may be computed in a manner similar to that used in the development of Equation 3.

$$U_1 = A_1 e^{j\omega_1 t}$$
$$U_2 = A_2 e^{j(\omega_2 t + \phi)}$$

Then the intensity, I, at the detector is:

$$I = |U_1 + U_2|^2 = (U_1^* + U_2^*)(U_1 + U_2)$$

$$=A_1^2+A_2^2+2A_1A_2\cos[(\omega_1-\omega_2)t+\phi]. \qquad (11)$$

The photodetector signal, then, is an offset sinusoid whose intensity varies at the difference frequency, $f=2\pi(\omega_1-\omega_2)$. When used in a Michelson interferometer configuration, a dynamic displacement of the object mirror results in a phase shift in the detected signal. Therefore, displacements are detected using electronic phase measurement techniques which can be made insensitive to signal amplitude variations.

Several techniques have been used to detect and process the phase shifted photodetector signal. Frequency demodulation has been used to measure the Doppler-shifted output signal (Whitman, Laub, and Bates, 1968). The doppler shifted frequency is proportional to the velocity of the surface motion and therefore electronic integration must be performed in order to obtain displacement information. The difficulties in accurately performing the required integration particularly at frequencies very near the difference frequency make Doppler frequency detection a less attractive option for heterodyne signal processing (Palmer and Green, 1979). FM detection using a phase locked loop has been used to successfully detect high frequency vibration and pulsed displacements (Rudd, 1980). In such a system an electronically phase locked loop is locked to the heterodyne signal from the photodetector. Phase variations occurring at a rate below the loop response rate (typically 100kHz) are tracked by the loop. Thus the output of the phase detector remains constant for low frequency phase changes. Since the frequency content of most environmental noise sources is well below 100kHz, the loop provides a level of noise immunity similar to that obtained with path length

stablilized interferometers. For vibrational disturbances above 100kHz, the error signal present at the output of the phase detector provides a voltage signal proportional to the velocity of the vibrational disturbance. Another scheme also sensitive to the velocity of the test object's surface displacement uses coherent detection of the phase shifted signal (DeLaRue, 1972). This technique works particularly well when the frequency of the acoustic exciting source is well known. In this case the signal to be detected is shifted to a sideband of the detector carrier frequency. By using the carrier signal as a local oscillator, immunity to environmentally induced path length instability is obtained. This optically derived local oscillator is then mixed with one of the signal sidebands to produce the desired output signal. In another coherent detection scheme for phase demodulation, the local oscillator is simply the input signal delayed by a known amount, typically $\approx$ 500ns (Jacobson, 1982). By delaying the local oscillator by some integral number of wavelengths plus $\lambda/4$, it can be made to be in quadrature with the heterodyne signal. Coherent detection using these two signals and subsequent filtering can be used to to provide a direct measure of phase. Again low frequency noise due to pathlength instability may be filtered out.

When changes in the detected phase difference occur slowly, direct phase measurement of the detected carrier frequency may be used. To do so requires a local oscillator source coherent with the detector signal. If the relative phase difference between the two is measured, then any change in the optical path difference between the reference and object beams will cause a corresponding change in the measured phase difference. Electronic phase difference measurements are quite easily and most commonly made using electronic instrumentation

which produces an analog output voltage proportional to the time between corresponding zero crossings of the two input signals expressed as a fraction of the signal period. This type of phase meter is capable of providing accuracies better than 0.1° (Mastner, 1980) thus giving a potential optical path difference sensitivity of $(\lambda/2)(0.1/360) = \lambda \times 1.4 \times 10^{-4}$ or about 0.07nm. For the work reported here, the relative phase differences between the signal and reference oscillator were derived from the outputs of a quadrature detection lock-in amplifier. Using a lock-in amplifier also reduces the effects of variations in input signal amplitude encountered with other phase measurement schemes (Ineichen, 1977).

Coherent quadrature detection for relative phase measurements is shown schematically in Figure 3. The input signal is mixed both with the local oscillator and with a 90° phase shifted version of the local oscillator.

Signal, $S = A\cos(\omega t + \phi) + N$

Local oscillator, $R_1 = B\cos\omega t$

Shifted L.O., $R_2 = B\sin\omega t.$

Output from first mixer is

$$O_1 = SR_1 = AB\cos\omega t\cos(\omega t+\phi) + NB\cos\omega t$$
$$= \left(\frac{AB}{2}\right)\cos(2\omega t+\phi) + \left(\frac{AB}{2}\right)\cos\phi + NB\cos\omega t.$$

Output from the second mixer is

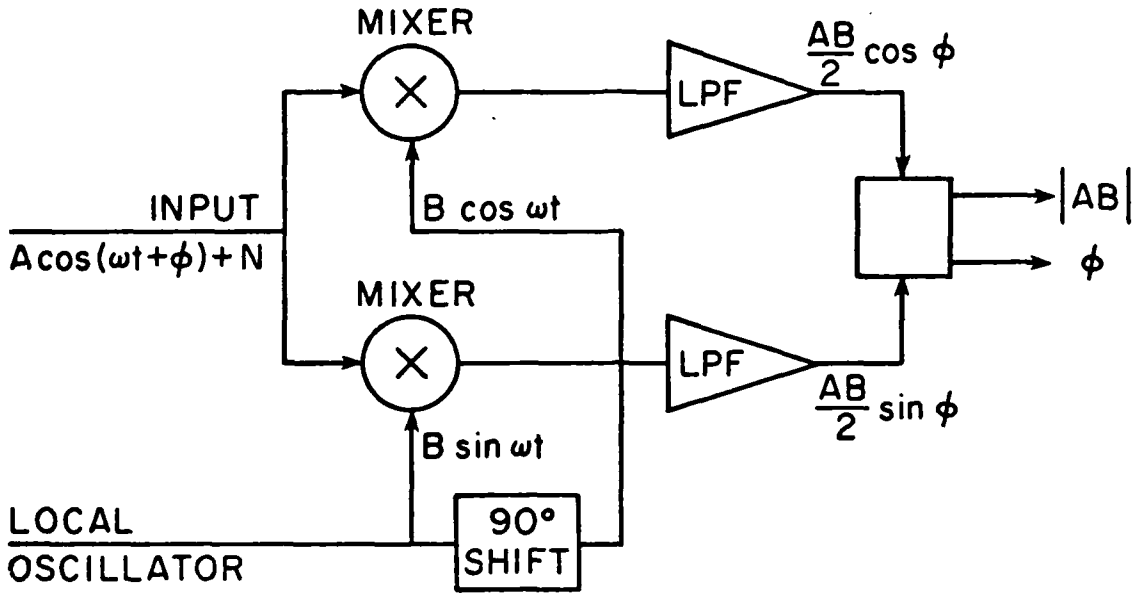

Figure 3: Lock-in Amplifier

$$O_2 = SR_2 = AB\sin\omega t\cos(\omega t+\phi) + NB\sin\omega t$$
$$= -\left(\frac{AB}{2}\right)\sin(2\omega t+\phi) - \left(\frac{AB}{2}\right)\sin\phi + NB\sin\omega t.$$

Note that by low pass filtering the outputs O_1 and O_2 only the second term in each expression is retained (assuming that $A_1 B_1$ and ϕ are slowly varying functions of time). Note also that the additive noise, N, originally present in the input signal is eliminated by this filtering process as well. In fact it is by this detection and filtering process that lock-in amplifiers may detect and amplify signals in noise backgrounds as much as 1000 times greater than the signal amplitude! The signals remaining after the filtering process then are as follows:

$$OF_1 = \frac{AB}{2}\cos\phi$$
$$OF_2 = \frac{AB}{2}\sin\phi$$

By taking the arctan of (OF_2/OF_1), the relative phase difference, ϕ, is computed. Some lock-in amplifiers are available which compute $\arctan(OF_2/OF_1)$ by an analog process in real time. Again owing to the coherent detection and filtering process, the ratio (OF_2/OF_1) and ϕ, therefore, is independent of the signal amplitude, A.

Judicious choice of the local oscillator source can reduce the effects of environmental noise on the accuracy of the relative phase measurement. The most commonly used technique for providing optical frequency shifting in heterodyne interferometry is the use of acousto-optic modulators, or Bragg cells. Other techniques which have been used include rotating diffraction gratings, rotating wave plates,

and electro-optical "serrodyning" (Hard, 1978; Aleksoff, 1971). Using a Bragg cell, the first order diffracted beams exiting the cell are shifted into upper and lower sidebands around the optical frequency ω. Light in either of the diffracted orders varies in frequency from the undiffracted beam by $\pm f_D$, where f_D is the RF driving frequency of the cell. The frequency shift is the result of a phenomenon known as the Debye-Sears effect (Adler, 1967). Typically the RF drive frequency for commercial Bragg cells is 40 or 80MHz. Therefore if an 80MHz Bragg cell is used to perform the frequency shifiting in a heterodyne interferometer, the difference frequency signal from the photodetector will be equal to the 80MHz drive frequency. While a high frequency carrier may be desirable in real-time detection of acoustic displacements, it is not necessary for the detection of slowly varying changes in optical path length. Indeed the design and construction of amplifiers and associated processing electronics becomes somewhat more complicated in the higher frequency regimes.

A more manageable carrier frequency is obtained by passing the laser beam through two Bragg cell modulators driven at slightly different frequencies as shown in Figure 4. Light diffracted into the +1 order of the first cell is frequency shifted upward by 80MHz. This first order diffracted beam passes subsequently through the second Bragg cell. The -1 order beam exiting the second cell is now shifted down in frequency by 80.1MHz. Therefore the net frequency shift caused by passing the beam through both cells is only 0.1MHz (100kHz). The resulting 100kHz difference frequency detected at the output of the heterodyne interferometer is far easier to amplify and process than would be the 80MHz. The diffraction efficiency of commercially available Bragg cell modulators using lithium niobate is better

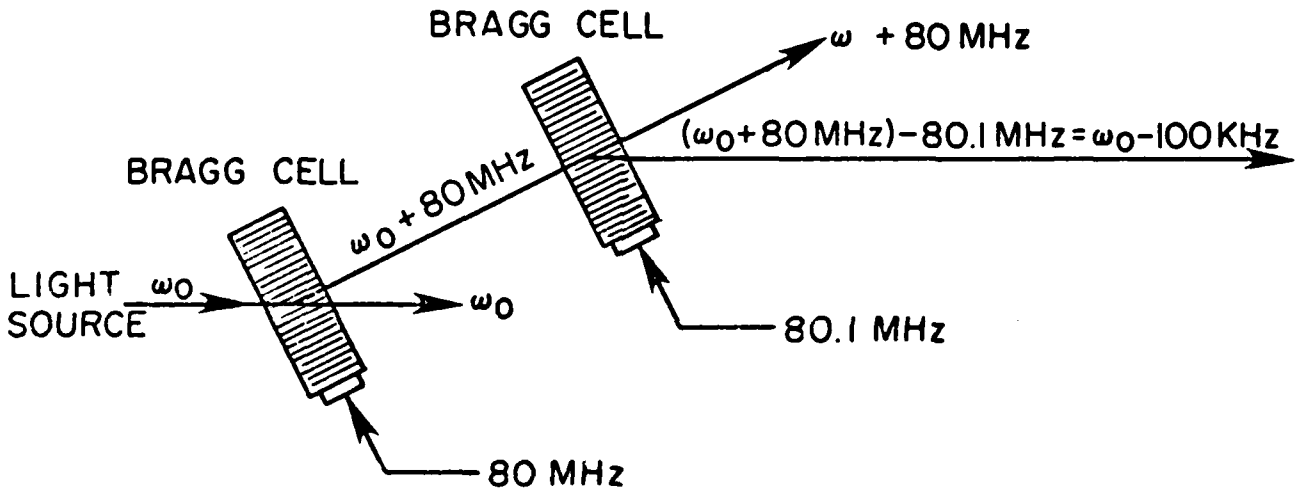

Figure 4: Obtaining a 100kHz frequency shift using two Bragg cells

than 80%. Consequently, the overall efficiency of this frequency shifting process is on the order of 65%. Unfortunately it is impractical to use just a single cell at 100kHz driving frequency because the diffraction efficiency would be quite poor, and more importantly, an extremely small diffraction angle of the 100kHz shifted components makes it difficult to spatially resolve the diffracted and undiffracted orders. There is, however, one very convenient feature of practical importance associated with using two Bragg cells for frequency shifting. That is the fact that both cells may be driven at the same shift frequency resulting in no net frequency shift nor causing any appreciable change in the optical path or angle through the cells. Therefore the heterodyne interferometer may be used in a homodyne mode without the need for reallignment of the beam in the shifted leg. This feature is particularly useful in initial allignment of the heterodyne interferometer.

Most of the discussion to this point has been with regard to the use of interferometers to detect and measure dynamic displacements at a single point on the surface of an object mirror. In fact, the research reported in this paper also addresses the problem of detecting and mapping dynamic surface displacements associated with traveling surface acoustic waves. However, unlike the interferometric techniques which have been discussed to this point, heterodyne holographic interferometry is not limited to real time surface displacement measurements at a single point on the test object. Instead, the surface displacements over the entire field of view of the test object are recorded at a single moment in time using pulsed holography. Subsequently, heterodyne interferometric techniques are applied to the reconstructed holographic image to provide details of the surface deformation over the entire field of view. This later step is quite similar to broad beam heterodyne

interferometry which has been used to measure surface flatness of optical components, for example.

In broad beam interferometry, the illuminating beams are expanded and collimated so that large surface areas may be interferometrically compared. If the object mirror is tilted or deformed relative to the reference mirror, a fringe pattern is generated in the output plane as shown in Figure 5. The fringes map out contours of constant displacement with a contour interval of $\lambda/2$. When a relative frequency shift is introduced between the reference and object beams, a detector placed in the output field generates a sinusoidal signal at the shift frequency. Direct measurement of the phase difference between this heterodyne signal and a local reference oscillator may then be used to interpolate between fringes providing a direct measure of out of plane displacement as a function of position on the object mirror surface. By scanning the detector over the output field, a map of surface topography may be generated. Such real-time broad beam, heterodyne interferometry has been used to measure flatness and curvature in mirrors, silicon wafers, and optical components (Massie, 1979).

Broad beam interferometry provides yet another possibility for reducing noise resulting from path instabilities in interferometry. A reference detector may be placed at any fixed point in the output field. The sinusoidal signal from this reference detector may be used as a local oscillator signal against which the phase of the signal from the scanning detector may be measured. Low frequency vibrational disturbances which may affect the optical pathlengths of either the reference or object leg of the interferometer will cause phase shifts in both the reference and

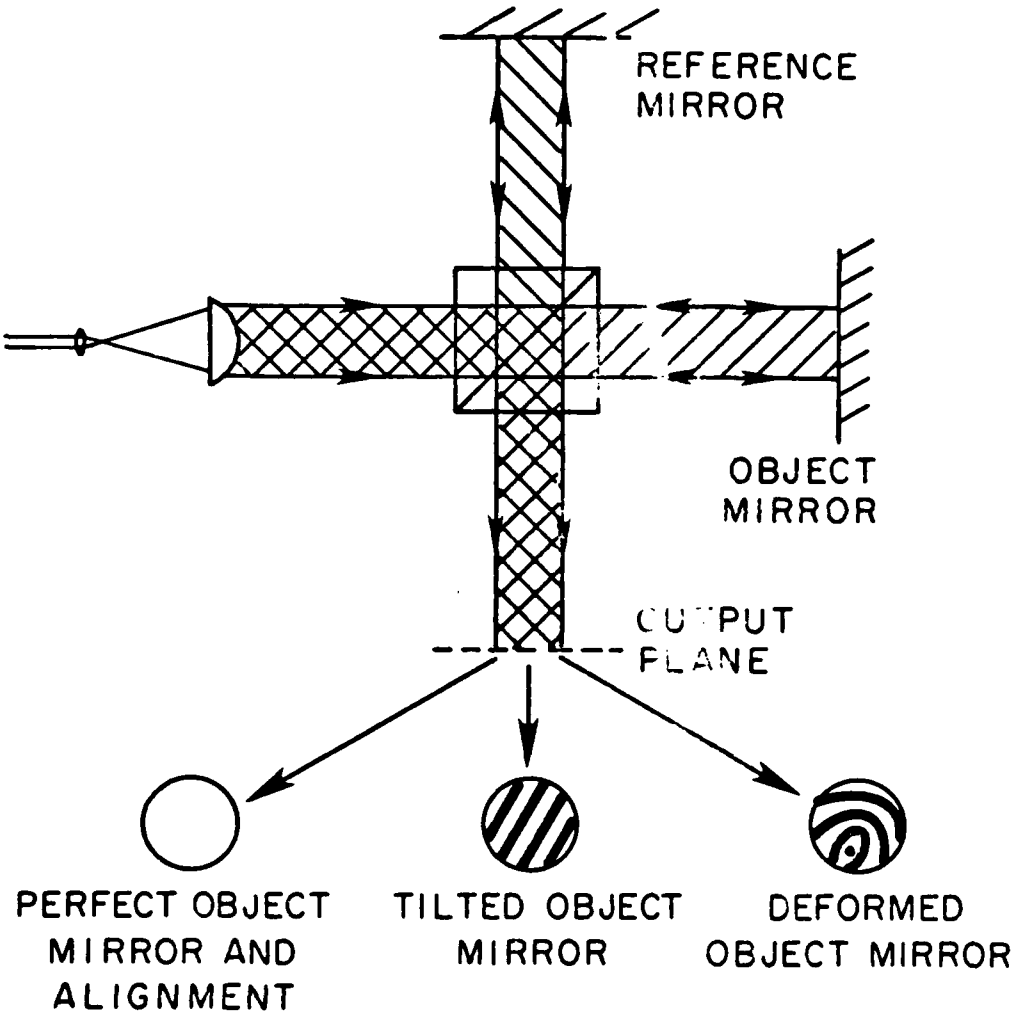

Figure 5: Broad beam interferometry
and examples of output patterns

scanning detector signals. Since both detectors are placed in the same output plane, the phase shifts resulting from vibration will be equal in both signals. Therefore the easured phase difference between the two signals will be unaffected by the vibrational disturbance.

Computing the noise limited sensitivity of a broad beam heterodyne interferometer requires an understanding of the effect of signal to noise ratio (SNR) on the performance of the system's phase meter. Assuming that the detector bandwidths are less than the heterodyne carrier frequency, then a phase error, $\Delta\phi$, using a zero-crossing phase meter is

$$\Delta\phi = \frac{1}{\sqrt{(SNR) f \tau}}$$

where τ = integration time

f = heterodyne frequency

(Ineichen, 1977).

If phase fluctuations from vibration and other environmental effects occur at frequencies outside of the system bandwidth, then the SNR can be assumed to depend only upon shot noise.

To compute the shot noise limited SNR, recall from Equation 11 that the light intensity incident on the photodetector is

$$P = P_0(1 + M\cos[(\omega_1 - \omega_2)t + \phi])$$

for $M=2A_1A_2/A_1^2+A_2^2$

and $P_0=A_1^2+A_2^2$.

The average power, P_0, contributes to the shot noise current while the signal current varies with the cosine term:

$$i_s=\frac{\eta q P_0}{h\nu}M\cos[(\omega_1-\omega_2)t+\phi]$$

$$\overline{i_S^2}=\frac{\eta^2 q^2 P_0^2 M^2}{2h^2\nu^2}$$

$$\overline{i_N^2}=2q\bar{i}B=2q\left(\frac{\eta q P_0}{h\nu}\right)B.$$

Therefore

$$SNR=\frac{\overline{i_S^2}}{\overline{i_N^2}}=\frac{\eta M^2 P_0}{4h\nu B}.$$

The phase error resulting from a shot noise limited system which incorporates a zero-crossing detector phase meter is

$$\Delta\phi=\frac{1}{\sqrt{(\eta M^2 P_0/4h\nu B)f\tau}}. \qquad (12)$$

Using the same values for η, M, P_0, and B as used earlier for the example calculation for the path-stabilized interferometer (i.e. $\eta = 0.3$, $M = 0.9$, $P_0=10^{-7}$ watts, and $B = 1$Hz) and using an Ar^+ laser ($\lambda = 0.5145$micron) and a zero-crossing

phase meter where $f\tau=1$, the phase error, $\Delta\phi$, for a heterodyne interferometer is 8×10^{-6} radians corresponding to a displacement sensitivity of about 0.003Å. Note that this is some 5 orders of magnitude better than was obtained for the path stabilized interferometer.

Holographic Interferometry

To this point, all discussion of interferometry, path stabilization, and detection has been illustrated by consideration of the Michelson interferometer. Holographic interferometry incorporates many of the same operating principles but reduces some restrictions imposed by classical interferometry, particularly regarding the types of specimens which may be examined. For any form of interferometry to be of practical use, the interference fringe pattern in the output plane must be of relatively low order so that individual fringes may be resolved. Obviously if the fringe rate is too high, there will be no fringe pattern observed visually or detected with a photodetector of finite area with dimensions larger than one fringe period. This necessity for a low fringe rate imposes the restriction that the two wavefronts to be interfered must be very nearly identical. In the case of a classical interferometer, nominally identical wavefronts are reflected from two flat mirrors with one mirror serving as a reference. When the object mirror is moved, tilted, or deformed, differences between the reference and object wavefronts occur which manifest

themselves in the observed interference pattern. If the object mirror is replaced by a diffusely reflecting surface, a very complicated and high fringe rate pattern appears in the output plane. The source of this complex pattern is clear if one considers that a diffusely reflecting surface is made up of a mosaic of small mirror-flat portions at random angles each reflecting a portion of the illuminating beam back to the output plane. Therefore the fringe pattern in the output plane is the result of interference of the light reflected from each of the individual reflectors with the reference beam as well as with each other. (It is the interference pattern from the interaction of the light from the individual surface reflectors with each other which is called speckle. The effects of speckle on the accuracy of holographic interferometry measurements will be discussed in some detail shortly.) By taking advantage of the "mosaic" nature of diffuse surfaces, one may still use classical interferometry to transduce surface displacements. This is often done by focusing the object illuminating beam down to a small point such that at the point of illumination the local variation of the object surface is negligible. The light is reflected directly back from the test point and recollimated by the focusing objective lens. Subsequent interference of this object beam with the reference takes place as though the beam were reflected from a flat mirror.

There are a number of applications, however, where it is desirable to interferometrically examine an entire surface. As discussed previously, broad beam interferometry may be used for objects with specularly reflecting surfaces which are either flat or of a known simple geometry. In such a system, a "master" object against which a test object is to be compared is used in place of a reference mirror. Usually wavefront correcting lenses are placed in each leg of the interferometer so

that the extent of the beams reflecting from each object can be controlled to stay within the physical dimensions of the components comprising the interferometer. The use of conventional spherical lenses restricts the nominal shapes of the test object surfaces to be either flat, convex, or concave.

Interferometric analysis of more complex, diffusely-reflecting surfaces requires that a reference wavefront be generated which matches that of the test object surface. One might consider the possibility of manufacturing a master object to replace the reference reflector in a Michelson interferometer as described above. It is important to remember, however, that in order for such an approach to work, every dimension of the master object including each minute reflector in the "mosaic" comprising the object surface must match that of the test object to be examined. It is certainly impractical, if not impossible, to produce reference surfaces with the required precision.

Holography provides one solution to the problem of generating a master wavefront for interferometric comparison of objects with arbitrary surface shape and texture. While some work has been done adapting holography for interferometric comparison of different, nominally identical objects (Neumann, 1981), by far the most common applications of holography in interferometry is in real-time or double-exposure interferometry where the object surface is compared at two different times. By interfering the wavefronts which reflect from the object both in a stressed and an unstressed state, for example, one may observe deformations which occur in the object as a result of applied stress. If the image of an object as recorded on a hologram is interfered with the image of the object at a slightly

different longitudinal magnification, the object appears superimposed with interference fringes forming contours of constant surface elevation.

The operating principles of holography may be explained using either wavefront interference theory from geometrical optics or alternatively using scalar diffraction theory. It is the latter approach which will be pursued here. In scalar diffraction theory, often called Fourier Optics (Goodman, 1968), an optical wavefront may be described as a complex quantity whose magnitude and phase varies as a function of x and y in a plane normal to the optical axix, z. A phasor notation of sorts may be used to explicitly specify the propagation direction of a wavefront as the angle between the propagation direction and the optical (z) axis as follows (Collier, 1971):

$$\hat{O} = Oe^{jf(\theta)} = Oe^{j\Phi}$$

where $\Phi = f(\theta) \alpha \theta$.

Looking at the optical set up shown in Figure 6, note that two wavefronts intersect at the film plate. One wavefront results from the reflection of the illuminating beam by the object surface and will be referred to as the object wavefront, $\hat{O}$. The second beam is unmodified by reflection and is called the reference beam, $\hat{R}$. Defining the optical axis to be perpendicular to the film plate:

$$\hat{R} = \underline{R}e^{j\Phi}$$
$$\hat{O} = \underline{O}e^{0} = \underline{O}.$$

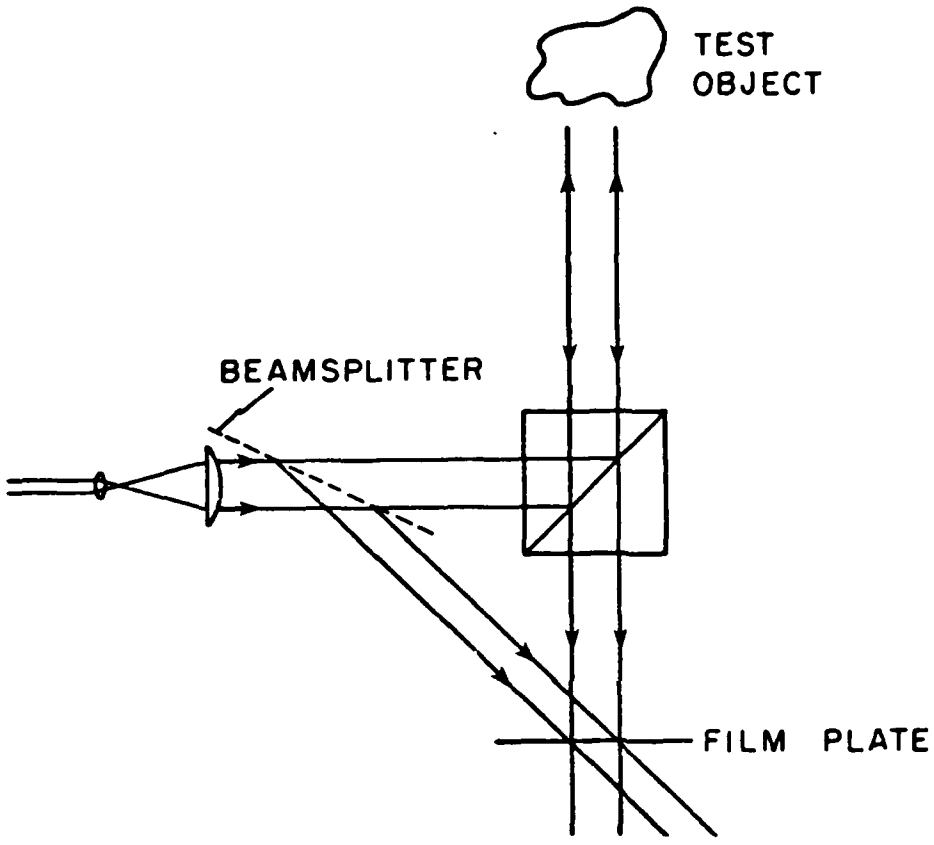

Figure 6: Holographic recording system.

Thus the optical field falling on the film plate, $A=\underline{R}e^{j\Phi}+\underline{O}$. Assuming that the transmittance, T, of the exposed and subsequently developed film is proportional to the field intensity, I, then:

$$\begin{aligned} T \propto I &= |A|^2 = |\hat{R}+\hat{O}|^2 \\ &= (\hat{R}+\hat{O})(\hat{R}^*+\hat{O}^*) \\ &= (\underline{R}e^{j\Phi}+\underline{O})(\underline{R}^*e^{-j\Phi}+\underline{O}^*) \\ &= |\underline{R}|^2+|\underline{O}|^2+\underline{O}\underline{R}^*e^{-j\Phi}+\underline{O}^*\underline{R}e^{j\Phi}. \end{aligned} \tag{13}$$

Upon reillumination by the reference beam as shown in Figure 7, the hologram diffracts the incident light into three beams corresponding to the three bracketed terms below.

$$T\times\underline{R}e^{j\Phi}=[(|\underline{R}|^2+|\underline{O}|^2)\underline{R}e^{j\Phi}]+[\underline{O}|\underline{R}|^2]+[\underline{O}^*|\underline{R}|^2e^{j\Phi}] \tag{14}$$

Analyzing Equation 14, the first term describes the intensity variations made to the reconstructing reference beam as it passes through the hologram plate and continues to propagate at an angle, θ, to the optical axis. The third term contains the conjugate image of the object and leaves the film plate at an angle 2θ relative to the optical axis. It is the second term of Equation 14 that is of importance in holographic interferometry. Note that this term describes a wavefront which propagates along the optical axis ($\Phi=\theta=0$) and is the product of the original object wavefront multiplied by the squared magnitude of the reference wavefront. In the case being considered here, the reference wave is a uniform, collimated beam such that its squared magnitude is simply a scalar constant independent of x and y. Thus a reconstructed replica of the original object wavefront propagates along the optical

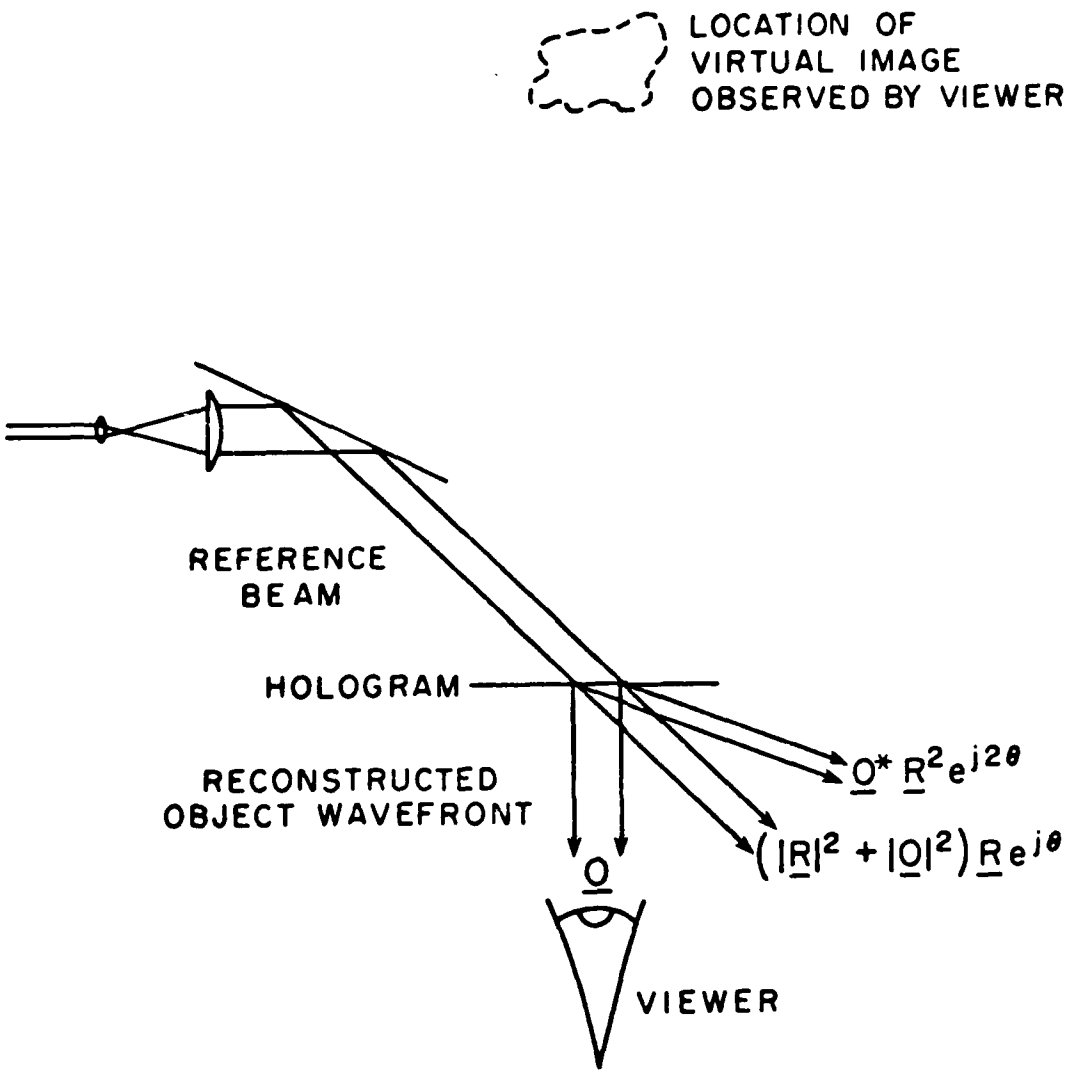

Figure 7: Wavefront reconstruction by holography.

axis such that an observer positioned as shown in Figure 7 would see a virtual image of the object appearing in its original location and in 3-D.

The holographically recorded image of the object may now be used as a "master" in an interferometer as shown in Figure 8. The recording and playback geometries shown in Figures 6, 7, and 8 were chosen to illustrate the similarity of holographic interferometry to the classical Michelson interferometer. In practice, however, off-axis illumination of the test object is used and the hologram serves as both a beam splitter and reference image source. Off-axis illumination does, however, complicate fringe analysis somewhat. Remember that interferometric fringe formation is the result of optical pathlength differences which occur between the reference and object wavefronts. For coaxial illumination, i.e. when the illumination and viewing axes are the same, one fringe corresponds to an object displacement of $\lambda/2$. For off-axis illumination, however, the sensitivity to object displacement is somewhat reduced. For analytical purposes a sensitivity vector, $\vec{K}$, is defined in the direction of the bisector of the illuminating and viewing axes (see Figure 9) (Vest, 1979). The sensitivity vector has a magnitude:

$$|\vec{K}| = 2k\cos\theta$$

where $k = \frac{2\pi}{\lambda}$

θ = half angle between the illuminating and viewing axes.

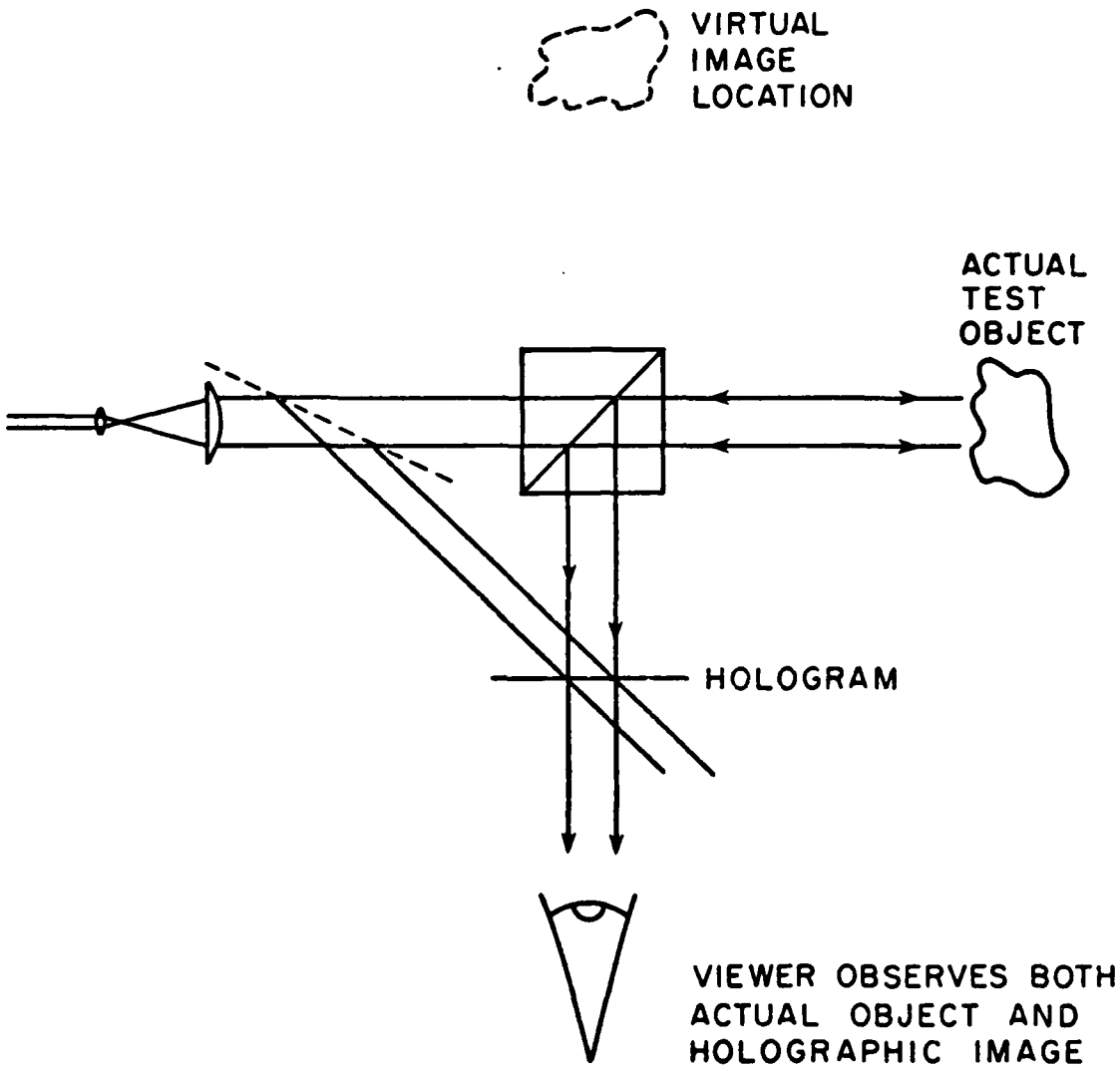

Figure 8: Holographic interferometry using coaxial illumination.

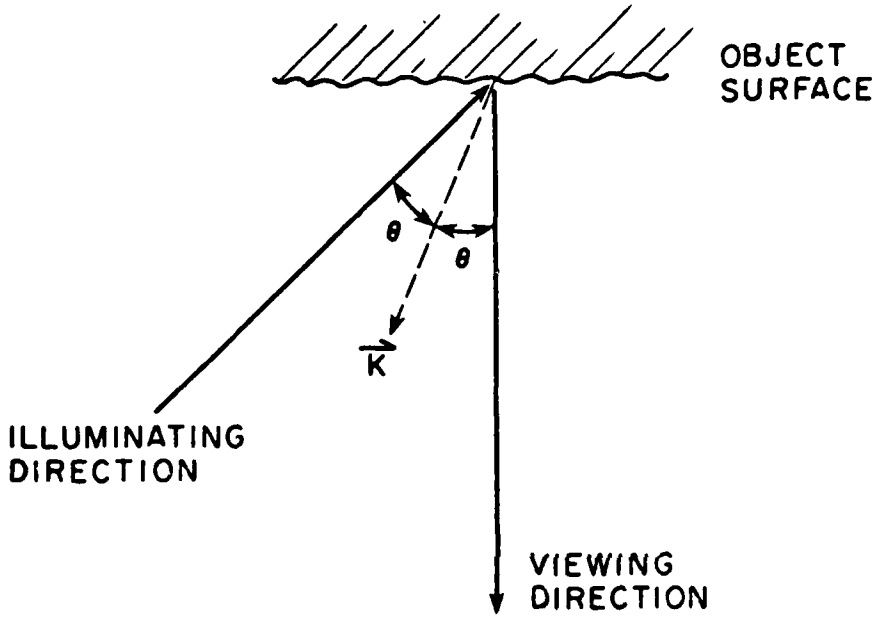

Figure 9: Sensitivity vector, K, for off-axis holographic interferometry.

For an object displacement $\vec{D}$, the observed intensity in the output plane of the holographic interferometer varies in a manner similar to that described in Equation 4 as follows:

$$I=2A^2(1+\cos\ \vec{K}\cdot\vec{D}) \qquad (15)$$
$$=2A^2[1+\cos(2kD\cos\theta\cos\phi)],$$

where ϕ is the angle between the sensitivity vector and the displacement direction, $\vec{D}$. Another advantage of holography is now apparent. Using Equation 15 the component of $\vec{D}$ in the $\vec{K}$ direction may be determined for any point on the object surface. By selecting three different viewing angles, the projection of $\vec{D}$ on three different $\vec{K}$ vectors may be computed and subsequently processed to completely specify $\vec{D}$ in magnitude and direction.

Double exposure holography eliminates the need to precisely replace and align the hologram in the optical set-up after its exposure and development. In this case, both the reference and object images are reconstructed by the hologram. The optical arrangement for recording a double exposure hologram can be identical to that used in real time holographic interferometry. Two exposures of the object image are recorded with a change either in magnification or applied stress being made between exposures. The alignment of the reference and object images is preserved in the hologram so that upon reconstruction with a single reference beam, both images are superimposed and therefore interfere. One variation of this double-exposure geometry is important in heterodyne applications. This variation is shown in Figure 10 where two spatially separated reference beams are used to record and reconstruct the holographic images. One reference beam and then the

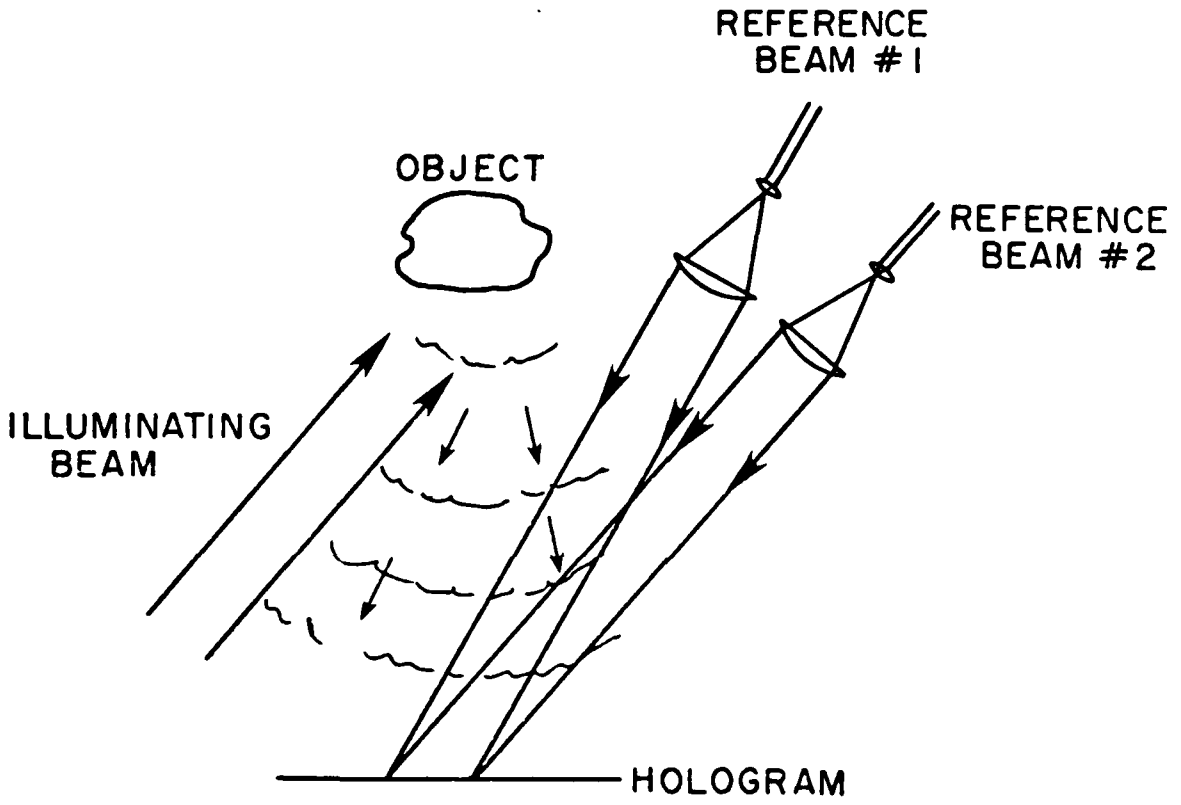

Figure 10: Dual reference beam holography
for heterodyne interferometry.

other is used in making the two exposures respectively. On playback, both beams are used to simultaneously reconstruct the reference and object images. If one of the reconstrucing reference beams is shifted in frequency relative to the other, then heterodyne analysis techniques similar to those used in broad beam heterodyne interferometry may be used.

Heterodyne Holographic Interferometry

Heterodyne analysis of dual reference beam, double exposure holograms recorded as described above, permits interpolation between the normally observed interferometric fringes. By interpolating between fringes both the sensitivity and dynamic range of holographic interferometry may be greatly improved. When first introduced in 1973, interpolation to better than 1/100 of a fringe was demonstrated (Dandliker, 1973). In 1980, Dandliker published a rather complete review paper on heterodyne holographic interferometry which predicts practical sensitivity limits of better than 1/1000 of a fringe (Dandliker, 1980). Indeed Dandliker and his associates dominate the literature from 1973 to 1980 on this topic. Consequently much of the theoretical development to be presented here is discussed in greater detail in his 1980 publication.

In many respects, the principles of heterodyne holographic interferometry

parallel those of broad beam heterodyne interferometry discussed earlier. In the holographic case, however, the two wavefronts to be interfered are reconstructed from the hologram plate rather than being reflected from reference and object mirror surfaces. By constructing the hologram with two reference beams as shown in Figure 10, the two reconstructed image wavefronts interfere only when both reference beams illuminate the developed hologram simultaneously. When one reference beam is shifted in frequency relative to the other, the two reconstructed image wavefronts are likewise shifted in frequency causing a corresponding variation in the image intensity. Mathematically, the transmittance of the dual reference beam, double exposure hologram can be expressed as the superposition of the transmittances which would result from each exposure independently as shown previously in Equation 13.

$$T \alpha |R_1|^2+|R_2|^2+|O_1|^2+|O_1^* R_1 e^{j\theta_1}+O_2^* R_2 e^{j\theta_2}+O_1 R_1^* e^{-j\theta_1}+O_2 R_2^* e^{-j\theta_2}, \quad (16)$$

where the subscripts, 1 and 2, refer to the first and second exposures, respectively. Again, only the last two terms will give rise to wavefronts which will propagate along the optical axis to the output plane.

To perform heterodyne analysis for fringe interpolation, the two reference beams used to reconstruct the object wavefront, O_1 and O_2, must be at slightly different frequencies. Let

$$\underline{R}_1 = R_1 e^{j(\omega_1 t+\theta_1)}$$
$$\underline{R}_2 = R_2 e^{j(\omega_2 t+\theta_2)}.$$

When together they illuminate the hologram whose transmittance is as shown in Equation 16, the light intensity falling on the output plane of the interferometer is obtained as follows:

$$\begin{aligned} I &= |(R_1+R_2)\times T|^2 \\ &= |O_2R_2^* e^{j(\omega_1 t+\theta_1-\theta_2)} \\ &\quad + O_1R_1^*R_2 e^{j(\omega_2 t+\theta_2-\theta_1)} \\ &\quad + O_2|R_2|^2 e^{j\omega_2 t} \\ &\quad + O_1|R_1|^2 e^{j\omega_1 t}|^2. \end{aligned}$$

If R_1 and R_2 are plane waves of unit amplitude then

$$I = |O_2 e^{j(\omega_1 t+\theta_1+\theta_2)} + O_1 e^{j(\omega_2 t+\theta_2-\theta_1)} + O_2 e^{j\omega_2 t} + O_1 e^{j\omega_1 t}|^2.$$

Note that only the last two terms of this expression correspond to wavefronts which propagate exactly down the optical axis toward the output plane. The first two terms form images which lie to either side of the optical axis propagating at an angle equal to that between the reference beams. Therefore considering only the last two terms above and noting that

$$O_1 = o_1 e^{j\phi_1(x,y)}$$
$$O_2 = o_2 e^{j\phi_2(x,y)}.$$

Then

$$I=|O_2e^{j(\omega_2t+\phi_2(x,y))}+O_1e^{j(\omega_1t+\phi_1(x,y))}|^2$$
$$=o_1^2+o_2^2+2o_1o_2\cos[(\omega_1-\omega_2)t+\phi_1-\phi_2]. \quad (17)$$

This is exactly the same form as obtained in Equation 11. Therefore sub-fringe interpolation between interferometric fringes may be accomplished at any point in the image by scanning a detector over the image plane and applying any of the phase detection schemes discussed previously.

Unlike the case of simple heterodyne interferometry, the resolution of heterodyne holographic interferometry is limited both by shot noise and speckle noise. If a zero-crossing phase meter is used to measure the phase difference between signals from two detectors located in the output plane, then the shot noise limited phase sensitivity is the same as that of broad beam heterodyne interferometry as expressed in Equation 12. To determine the effect of speckle on the accuracy of phase measurements it is helpful to understand some of the statistical properties of speckle. The discussion which follows is not intended to provide a complete description of speckle phenomena but rather will attempt to develop those properties of speckle which directly affect the accuracy of heterodyne holographic interferometry.

Speckle is the name given to the phenomenon which gives a granular appearance to diffusely reflecting (or transmitting) objects illuminated by a coherent source. The origin of speckle is quite easily explained when one considers that a diffusely reflecting (rough) surface can be considered to be composed of a mosaic of mirror-flat sections whose dimensions are on the order of the wavelength of the

illuminating light and whose faces are oriented randomly about the average surface normal. At any point in front of such an object, light from the illuminating source is scattered by a number of surface reflectors creating a complex interference pattern. In general, this speckle pattern is observed using an imaging system such as the eye or a camera so that there is a finite aperture through which the light must pass before it is focused on the image plane. This finite aperture limits the resolution of the imaging system thus establishing the speckle size at that limit. Consequently for a square or a circular aperture, the speckle size is $\lambda z/d$ or $1.22\lambda z/D$, respectively, where z is the distance from the aperture to the image plane and D is the aperture width (Jenkins and White, 1950). The results of this rather intuitive argument for determining speckle size agree with those obtained by more rigorous analysis (Dandliker, 1980; Vest, 1979; Goodman, 1975). Speckle size, as will be shown shortly, is an important factor in determining fringe contrast of holographic interferograms.

As discussed earlier, the only practical way to interfere wavefronts reflecting from diffuse object surfaces is through holographic interferometry. In the mathematical description of the two reflected fields, a roughness term, ρ, must be added to account for the microscopic variations in surface topography which give rise to speckle. Therefore the two wave fields are expressed as follows:

$$A_1 = a_1(\underline{x}_0)\rho_1(\underline{x}_0)$$
$$A_2 = a_2(\underline{x}_0)\rho_1(\underline{x}_0),$$

where a_1 and a_2 represent the macroscopic, or smooth, variations in the reflected wavefront and $\underline{x}_0 = (x_0, y_0)$ positions in the object plane. On the output plane of a

linear space-invarient imaging system, the complex amplitude of each wavefront may be computed by convolution with the impulse response of the imaging system, $h(\underline{x})$:

$$B_1(\underline{x}_i)=\int a_1(\underline{x}_0)\rho_1(\underline{x}_0)h(\underline{x}_i-M\underline{x}_0)d\underline{x}_0 \qquad (18)$$
$$B_2(\underline{x}_i)=\int a_2(\underline{x}_0)\rho_2(\underline{x}_0)h(\underline{x}_i-M\underline{x}_0)d\underline{x}_0,$$

where $\underline{x}_i=(x_i,y_i)$ positions in the image, or output, plane of the imaging system and M is the lateral magnification of the system. The intensity in the image plane is the coherent superposition of the wavefronts B_1 and B_2 such that

$$I=|B_1+B_2|^2=|B_1|^2+|B_2|^2+B_1B_2^*+B_2B_1^*.$$

As always, the last two terms represent the interference of the two wavefronts. To separate the microscopic (speckle) interference from the macroscopic interference it is useful to examine the average interference field over a large number of diffusers, ρ. The emsemble average of the interference terms may be expressed as

$$<B_1B_2^*+B_2B_1^*>.$$

However, since $<B_1B_2^*>=<B_2B_1^*>$, the overall average will be twice the average of either term. Therefore consider

$$<B_1B_2^*>=<(\int a_1(\underline{x}_0)\rho_1(\underline{x}_0)h(\underline{x}_1-M\underline{x}_0)d\underline{x}_0)\times(\int a_2^*(\underline{x}_0)\rho_2^*(\underline{x}_0)h^*(\underline{x}_i-M\underline{x}_0)d\underline{x}_0)>.$$

By changing the dummy variable in the second integral to $\underline{x}_0'$, the order of multiplication and integration may be reversed such that

$$<B_1B_2^*>=<\int\int a_1(\underline{x}_0)a_2^*(\underline{x}_0')\rho_1(\underline{x}_0)\rho_2^*(\underline{x}_0')h(\underline{x}_i-M\underline{x}_0)h^*(\underline{x}_i-M\underline{x}_0')d\underline{x}_0d\underline{x}_0'>.$$

Finally, ρ_1 and ρ_2 are considered to be ergodic random processes which is to say that the statistical properties of the roughness over any sample area of the object surface are equal to those obtained for any other sample area. Consequently it is permissible to reverse the order with which the integration and averaging is performed (Lathi, 1968) so that

$$<B_1B_2^*>=\int\int a_1(\underline{x}_0)a_2^*(\underline{x}_0')<\rho_1(\underline{x}_0)\rho_2^*(\underline{x}_0')>h(\underline{x}_i-M\underline{x}_0)h^*(\underline{x}_i-M\underline{x}_0')d\underline{x}_0'd\underline{x}_0 \quad (19)$$

Through Equation 19 it is possible to demonstrate a great deal about the effect of surface roughness and speckle on the interference of two diffusely reflected wavefronts. First, to convince oneself of the physical significance of Equation 19, consider the case where $B_1=B_2$, then

$$<B_1B_2^*>=<B_1B_1^*>=<|B_1|^2>,$$

which is the average intensity of B_1 in the output plane of the imaging system. Since $B_1=B_2$ then $\rho_1=\rho_2$. Thus $<\rho_1(\underline{x}_0)\rho_1^*(\underline{x}_0)>$ is the autocorrelation of the surface roughness $R_\rho(\underline{x}_0-\underline{x}_0')$. Recall that the spatial frequency spectrum of the surface roughness is assumed to extend well beyond the bandwidth of the imaging system. In other words the fine detail of the surface cannot be resolved by the im-

aging system. Therefore the autocorrelation peak of the surface roughness will be much narrower than the resolution of the imaging system and can be approximated by a delta function:

$$<\rho_1(\underline{x}_0)\rho_1(\underline{x}_0')>\approx\delta(\underline{x}_0-\underline{x}_0').$$

Owing to the shifting property of the delta function, Equation 19 is considerably simplified,

$$\begin{aligned}<|B|^2>=&\int\int a_1(\underline{x}_0)a_1^*(\underline{x}_0')h(\underline{x}_i-M\underline{x}_0)\\&\times h^*(\underline{x}_i-M\underline{x}_0)\delta(\underline{x}_0-\underline{x}_0')d\underline{x}_0d\underline{x}_0'\\=&\int|a_1|^2(\underline{x}_0)|h|^2(\underline{x}_i-M\underline{x}_0')d\underline{x}_0'.\end{aligned}$$

The above expression is now recognized as the convolution of the input intensity, $|a|^2$, with the incoherent transfer function.

Having established the physical significance of Equation 19, return now to the interference case where $B_1\neq B_2$. First observe that, for interference to exist at all, the roughness terms for the two wavefronts must be correlated, i.e. $<\rho_1(\underline{x}_0)\rho_2^*(\underline{x}_0')>\neq 0$. In practice, then, one can interfere two speckle fields only if both wavefronts originate by reflection from the same object surface in two different states. This explains the value of holography in performing interferometric analysis of diffuse object surfaces. Assume that following the recording and subsequent development of a hologram, the test object is translated by an amount $\underline{u}$ as shown in the real time holographic interferometer of Figure 11. The interference term (Equation 19) will be affected in two ways. First, B_2 will be

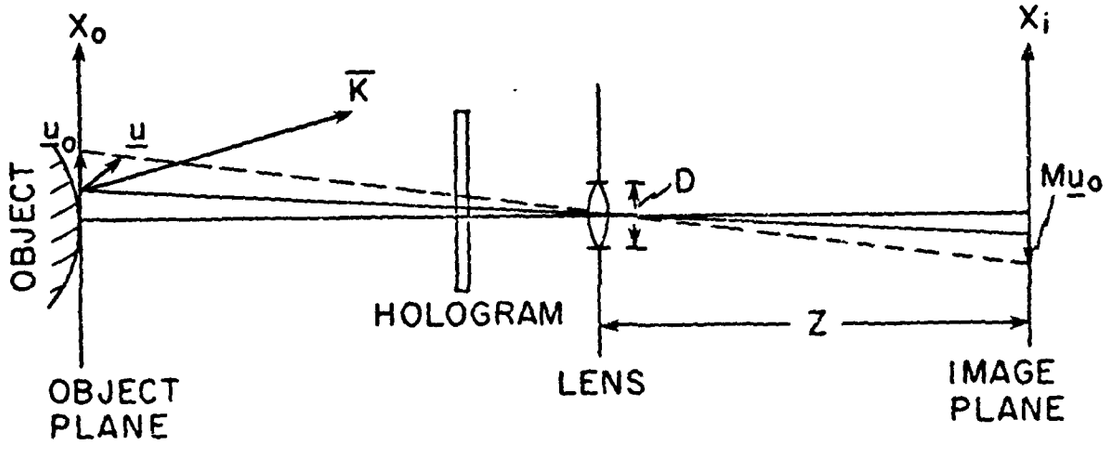

Figure 11: Real time holographic interferometer.

shifted in phase by an amount equal to the projection of $\underline{u}$ on the sensitivity vector, $\vec{K}$ (see Figure 9). Secondly, there will be a lateral shift in the speckle field of B_2 in the image plane by an amount equal to the product of the lateral magnification, M, and the projection of $\underline{u}$ on $\underline{x}_0$. Thus

$$\begin{aligned} B_2(\underline{x}_i) &= B_1(\underline{x}_i + M(\underline{u}\cdot\underline{x}_0))e^{j(\vec{k}\cdot\underline{u})} \\ &= B_1(\underline{x}_i + \underline{u}_i)e^{j\phi}, \end{aligned}$$

where

$$\underline{u}_i = M(\underline{u}\cdot\underline{x}_0)\phi = \vec{K}\cdot\underline{u}.$$

Substituting into Equation 18:

$$B_I = e^{j\phi}\int a_1(\underline{x}_0)\rho_1(\underline{x}_0)h(\underline{x}_i + \underline{u}_i - M\underline{x}_0)d\underline{x}_0.$$

So that Equation 19 becomes

$$\begin{aligned} \langle B_1 B_2^* \rangle &= e^{j\phi}\int\int a_1(\underline{x}_0)a_1^*(\underline{x}_0)\langle \rho_1(\underline{x}_0)\rho_1^*(\underline{x}_0')\rangle h(\underline{x}_i - M\underline{x}_0)h^*(\underline{x}_i + \underline{u}_i - M\underline{x}_0)d\underline{x}_0' d\underline{x}_0 \\ &= e^{j\phi}\int\int a_1(\underline{x}_0)a_1^*(\underline{x}_0')h(\underline{x}_i - M\underline{x}_0)h^*(\underline{x}_i + \underline{u}_i - M\underline{x}_0)\delta(\underline{x}_0 - \underline{x}_0')d\underline{x}_0' d\underline{x}_0 \\ &= |a_1|^2(\underline{x}_0')e^{j\phi}\int h(\underline{x}_i - M\underline{x}_0)h^*(\underline{x}_i + \underline{u}_i - M\underline{x}_0')d\underline{x}_0' \\ &= |a_1|^2(\underline{x}_0')e^{j\phi}R_h(\underline{u}_i), \end{aligned}$$

where $R_h(\underline{u}_i)$ is the autocorellation of the coherent impulse response, h. This autocorrelation is also the impulse response function or point spread diameter and determines the resolution of the imaging system which is the speckle size. For a

circular aperture, the autocorrelation function is an Airy function whose value is a maximum for $\underline{u}_i=0$ and falls to zero when $\underline{u}_i=1.22\lambda/D$. Therefore the interference fringes will be visible only for lateral shifts of the speckle pattern, $\underline{u}_i$, which are less than the resolution limit of the imaging system. The fringe contrast, γ, can then be defined:

$$\gamma(\underline{u}_i)=|R_h(\underline{u}_i)|\leq 1. \tag{20}$$

With the development of the concept of fringe contrast it is now possible to address the effect of speckle on the accuracy of phase measurements in heterodyne holographic interferometry. Since γ takes into account effects of the imaging system, it is no longer necessary to define the output wavefronts B_1 and B_2 in terms of the input fields and the system transfer function. Instead let

$$\begin{aligned} B_1(\underline{x},t)&=b_1(\underline{x})v_1(\underline{x})e^{j\omega_1 t} \\ B_2(\underline{x},t)&=b_2(\underline{x})v_2(\underline{x})e^{j(\omega_2 t+\phi(x))}, \end{aligned} \tag{21}$$

where b_1 and b_2 are the average macroscopic image amplitudes and v_1 and v_2 are complex variables related to the object surface roughness and the resulting speckle fields. In order for B_1 and B_2 to interfere, however it is necessary that v_1 and v_2 be somewhat correlated, thus v_2 can be considered to be the sum of two uncorrelated fields whose magnitudes are dependent on the contrast, γ (Dandliker, 1980):

$$v_2(\underline{x})=\gamma v_1(\underline{x})e^{j\phi}+(1-\gamma^2)^{1/2}w(\underline{x})$$

$$\langle|v_1|^2\rangle=\langle|v_2|^2\rangle=1$$
$$\langle v_1 v_1^*\rangle=R_n(\underline{u})$$
$$\langle v_1 w^*\rangle=0$$
$$\langle|v_1|^4\rangle=2.$$

Substituting into Equation 21:

$$B_1(\underline{x},t)=b_1(\underline{x})v(\underline{x})e^{j\omega_1 t}$$
$$B_2(\underline{x},t)=b_2(\underline{x})[\gamma v(\underline{x})e^{j\phi}+(1-\gamma^2)^{1/2}w(\underline{x})]e^{j\omega_2 t}.$$

The interference term of the intensity:

$$B_1^* B_2 \alpha[\gamma v v^* e^{j\phi}+(1-\gamma^2)^{1/2}v^* w]e^{j(\omega_2-\omega_1)t}, \qquad (22)$$

where the first term is the correlated term and the second is an uncorrelated term which will add randomly to the coherent term introducing a phase error $\Delta\phi$. For a detector area large enough only to receive light from two speckles, the vector diagram in Figure 12 applies. The net uncorrelated component is the vector sum of the random uncorrelated components of each speckle. The correlated components add coherently resulting in a net component equal to the sum of the individual components from each speckle. One can see then that the phase error, $\Delta\phi$, will be reduced as the number of speckles falling on the detector increases. From the figure, the phase error can be expresses as

$$\sin\Delta\phi=\frac{i_u \sin\psi}{i_c}.$$

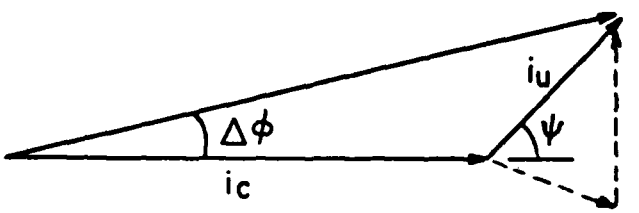

Figure 12: Vector diagram of speckle addition.

For small phase errors $\sin\Delta\phi = \Delta\phi$, so the mean square phase error is

$$\langle\Delta\phi^2\rangle = \frac{\langle|i_u|^2\sin^2\psi\rangle}{\langle|i_c|^2\rangle} = \frac{1}{2}\frac{\langle|i_u|^2\rangle}{\langle|i_c|^2\rangle}.$$

To compute $\Delta\phi$ as a function of the number of speckles, N, on the detector, it is necessary to find expressions for $\langle|i_c|^2\rangle$ and $\langle|i_u|^2\rangle$. From Equation 22

$$\begin{aligned}
\langle|i_c|^2\rangle &= \sum_{n=m=1}^{N}\langle i_{c_n} i_{c_m}^*\rangle \\
&= \gamma^2\sum_{n=m=1}^{N}\langle v_n v_n^* v_m^* v_m\rangle \\
&= \gamma^2(N\langle|v|\rangle + N(N-1)\langle|v|^2\rangle^2 \\
&= \gamma^2 N(N+1); \\
\langle|i_u|^2\rangle &= \sum_{n=m=1}^{N}\langle i_{u_n} i_{u_m}^*\rangle \\
&= (1-\gamma^2)\sum_{n=m=1}^{N}\langle v_n w_n^* v_m w_m\rangle \\
&= (1-\gamma^2)N\langle|v|^2\rangle\langle|w|^2\rangle \\
&= (1-\gamma^2)N,
\end{aligned}$$

and finally:

$$\begin{aligned}
\langle\Delta\phi^2\rangle &= \frac{1}{2}\frac{\langle|i_u|^2\rangle}{\langle|i_c|^2\rangle} \\
&= \frac{1}{2}\frac{N(1-\gamma^2)}{\gamma^2 N(N+1)} \\
&= \frac{(1-\gamma^2)}{\gamma^2(N+1)}.
\end{aligned}$$

Thus, the RMS phase error is

$$\Delta\phi = \left[\frac{1-\gamma^2}{\gamma^2(N+1)}\right]^{1/2}. \tag{23}$$

The use of two reference beams to record a double exposure hologram for subsequent heterodyne analysis introduces two additional parameters whose effects may degrade the accuracy of the phase measurements. These two parameters are misalignment of the reconstructing reference beams and wavelength differences between the recording and reconstruction sources. Both are pertinent to this work since in the final experiments holograms were recorded and analyzed in two separate optical systems. In addition a frequency-doubled Nd:YAG laser (λ=532nm) was used to record the holograms while reconstruction and analysis was performed using the 514.5nm line of an argon ion laser.

Although Dandliker discusses effects of misalignment and wavelength in his 1980 review paper, the physical significance of these effects is easily lost in the mathematics associated with k-space manipulations and scalar diffraction theory. For this reason, the following development is offered using geometrical optics theory of diffraction gratings. While this approach does not appear in the literature, it is never-the-less appropriate for this background discussion.

In one sense, a hologram is a spatial-frequency moduated diffraction grating whose carrier frequency is determined by the angle between the reference beam and the average object beam direction. In the case of a dual reference beam holo-

gram, two independent diffraction gratings are recorded on the hologram - one for each exposure. Given that the hologram may be treated as a complex diffraction grating, it becomes clear then that any angular misalignment or wavelength change will cause a change in the angles of the diffracted beams exiting the hologram. Angular changes result in lateral shifts of the images formed in the output plane of the interferometer. Such lateral shifts cause a reduction in fringe contrast according to Equation 10 which in turn degrades the phase accuracy as shown in Equation 23.

To quantitate these effects, consider the hologram geometry shown in Figure 13 where R_1 and R_2 are plane waves. The hologram is drawn as a broken line symbolic of its diffraction grating nature. An imaging lens is located as close to the hologram plate as possible. Assuming perfect alignment of the reconstructiang reference beams, R_1 and R_2, and further assuming no change in optical wavelength between hologram recording and reconstruction, the reconstructed object beams, O_1 and O_2, propagate at an angle θ_f to the hologram (grating) normal and are imaged on the output plane where they interfere. The propagation angles for R_1, O_1, R_2, and O_2 obey the grating equation for first order diffraction:

$$\lambda = a(\sin\beta_R + \sin\beta_O),$$

where the β angles are measured with respect to the grating normal and a is the grating spacing. In the case diagramed in Figure 13:

$$\lambda = a_1(\sin(\theta_1 - \delta) + \sin\theta_f) \qquad (24)$$

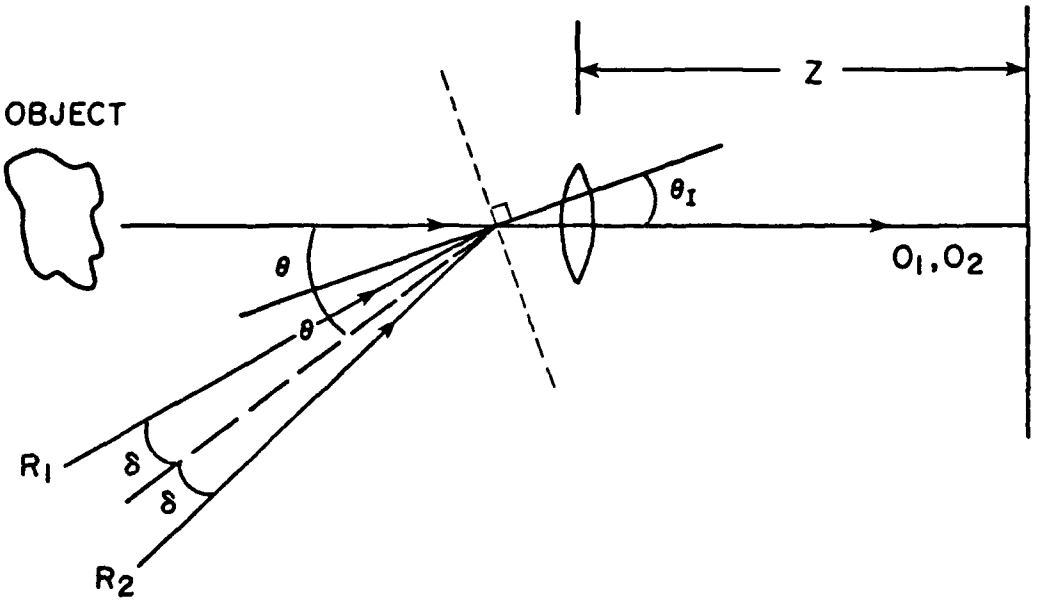

Figure 13: Holographic set-up.

$$\lambda = a_2(\sin(\theta_2+\delta)+\sin\theta_I)$$

Consider the case when both reference beams are slightly misaligned such that each is displaced angularly from its bisector by an additional amount $\Delta\delta$. In this case for R_1 the change in θ_I may be computed by direct application of Equation 24:

$$\sin\theta_I - \sin(\theta_I+\Delta\theta_I) = [\frac{\lambda}{a_1} - \sin(\theta-\delta)] - [\frac{\lambda}{a_1} - \sin(\theta-(\delta+\Delta\delta))]$$

$$2\cos\frac{1}{2}(2\theta_I+\Delta\theta_I)\sin\frac{1}{2}(-\Delta\theta_I) = \sin(\theta-\delta-\Delta\delta) - \sin(\theta-\delta)$$

$$= 2\cos\frac{1}{2}(2\theta-2\delta-\Delta\delta)\sin\frac{1}{2}(-\Delta\delta).$$

If $\Delta\delta$ is small, then

$$-\Delta\theta_I\cos\theta_I \approx -\Delta\delta\cos(\theta-\delta)$$

$$\Delta\theta_I = \Delta\delta\frac{\cos(\theta-\delta)}{\cos\theta_I}.$$

Similarly for R_2,

$$\Delta\theta_{I_2} = -\Delta\delta\frac{\cos(\theta-\delta)}{\cos\theta_I}.$$

The total angular separation between the two reconstructed object beams is

$$\Delta\theta_I = \Delta\theta_{I_1} - \Delta\theta_{I_2}$$

$$= \Delta\delta\frac{1}{\cos\theta_I}[\cos(\theta-\delta)+\cos(\theta+\delta)]$$

$$-\frac{\Delta\delta}{\cos\theta_I}\left[2\cos\frac{1}{2}(-2\delta)\cos\frac{1}{2}(2\theta)\right]$$

$$-2\Delta\delta\frac{\cos\theta}{\cos\theta_I}\cos\delta$$

$$-2\Delta\delta\cos\delta \quad \textit{since } \theta_I=\theta.$$

The corresponding translation in the image plane is

$$u_I=\Delta\theta_I z \qquad (25)$$
$$=2z\,\Delta\delta\cos\delta.$$

For a practical system using a circular imaging aperture so that

$$\gamma=\frac{2}{\pi u_I D/\lambda z}J_1\left(\frac{\pi u_I D}{\lambda z}\right)$$

and λ=514.5nm, z=15cm, D=7.5cm, δ=5°, the maximum angular misalignment, $\Delta\delta$, which will still result in a fringe contrast γ=0.7 may be computed since γ=0.7 corresponds to $u_I D/\lambda z$=0.5. By substitution, u_I is found to be equal to the wavelength (514.5nm). Solving Equation 25 for $\Delta\delta$, the maximum angular misalignment is found to be about 10^{-4}degrees! Such fine alignments are achievable with precision optical mounts. However, this result helps explain why frequent realignment is required with changes in the ambient temperature of the laboratory.

Sensitivity to wavelength changes can likewise be analyzed using the diffraction grating analogy and Figure 13. This time it will be assumed that $\Delta\delta$=0 and that a

different wavelength is used for reconstructing the holographic images than was used to record the hologram. The reconstruction angle, θ_I, is shifted when the hologram is reconstructed using λ_2 from what it would have been if reconstructed using λ_1 by an amount which may be computed using Equation 24:

$$\sin\theta_I - \sin(\theta_I + \Delta\theta_I) = \left[\frac{\lambda_1}{a_1} - \sin(\theta - \delta)\right] - \left[\frac{\lambda_2}{a_2} - \sin(\theta - \delta)\right]$$

$$-\Delta\theta_I \cos\theta_I = \frac{1}{a_1}(\lambda_1 - \lambda_2)$$

$$\Delta\theta_{I_1} = -\frac{1}{a_1 \cos\theta_I}(\lambda_1 - \lambda_2).$$

The same result is obtained for the second reference beam indicating as expected that θ_I will be shifted in the same direction for both cases. Therefore the total shift in θ_I is the difference between the two:

$$\Delta\theta_I = \Delta\theta_{I_1} - \Delta\theta_{I_2}$$

$$= -\frac{\lambda_1 - \lambda_2}{a_1 \cos\theta_I} - \frac{\lambda_1 - \lambda_2}{a_1 \cos\theta_I}$$

$$= -\frac{\lambda_1 - \lambda_2}{\cos\theta_I}\frac{a_1 - a_2}{a_1 a_2}.$$

From Bragg's equation

$$a_1 = \frac{\lambda_1}{2\sin\frac{1}{2}(2\theta - \delta)}$$

$$a_2 = \frac{\lambda_1}{2\sin\frac{1}{2}(2\theta - \delta)}$$

$$\frac{a_1 - a_2}{a_1 a_2} = \frac{\lambda_1 2\sin\frac{1}{2}(2\theta + \delta) - \lambda_1 2\sin\frac{1}{2}(2\theta - \delta)}{\lambda_1^2}$$

$$=\frac{2}{\lambda_1}\left[\sin\frac{1}{2}(2\theta+\delta)-2\sin\frac{1}{2}(2\theta-\delta)\right]$$

$$=\frac{2}{\lambda_1}\left[2\cos\frac{1}{2}(2\theta)\sin\frac{1}{2}(\delta)\right].$$

Thus

$$\Delta\theta_I=4\frac{\lambda_1-\lambda_2}{\lambda_1}\frac{\cos\theta}{\cos\theta_I}\sin\frac{\delta}{2}$$

$$=4\frac{\lambda_1-\lambda_2}{\lambda_1}\sin\frac{\delta}{2} \quad \textit{since } \theta_I=\theta.$$

Finally,

$$u_I=z\,\Delta\theta_I=4z\frac{\lambda_1-\lambda_2}{\lambda_1}\sin\frac{\delta}{2}. \tag{26}$$

Note that for a single reference beam, i.e. $\delta=0$, there is no shift in θ_I for a change in λ so double exposure single reference beam holograms are readily reconstructed using any laser wavelength without loss of fringe contrast. Again for the specific experiment to be discussed later, $\lambda_1=532$nm and $\lambda_2=514.5$nm. For a fringe contrast $\gamma=0.7$, the u_I is 514.5nm as before. Using Equation 26 it is found that δ must be less than 3×10^{-3}degrees. Such a small separation between reference beams would cause overlap of the interfering image with the secondary images which were neglected in the development of Equation 17. These additional uncorrelated images add to the background illumination of the image field thus cutting the effective γ in half and adding to the noise power of the detector.

Pulsed Holography

Holographic recording using pulsed lasers has been used to reduce the effects of environmental vibration or object motion on holographic quality over a broad range of applications from holographic portraiture to nondestructive testing (Collier, 1971b). Nondestructive testing applications include contouring, vibrational mode analysis, and transient stress and deformation analysis (Gagosz, 1974; Chu, 1972; Albe, 1976). In the area of transient analysis, pulsed holography has been employed to "freeze" the motion of relatively large amplitude acoustic waves including plate waves and Rayleigh waves (Aprahamian, 1971; Gagosz, 1974). In both of these studies, however, the surface displacements were sufficient to be visible using single reference beam double exposure holographic interferometry. They are significant to this study in that they demonstrate that surface displacements, and rate of displacement in particular, associated with acoustic waves is insufficient to cause noticable reduction of holographic efficiency. Indeed the reduction of holographic efficiency may be computed directly for objects in uniform and/or vibrational motion if the laser pulse duration, pulse shape, and the component of object velocity along the sensitivity vector is known (Gustafson, 1980). Using Gustafson's formulas, the reduction of holographic efficiency resulting from the subfringe displacements encountered in this work would be less than 0.5%.

Although the reconstruction efficiency is not significantly reduced by small acoustic perturbations of the object surface, the accuracy with which such perturbations are recorded remains in question. Unfortunately the answer to this question is not available in the literature at present. However an argument can be presented based on the supposition that one cannot expect recorded phase accuracy any greater than that associated with the object displacement which takes place during the laser pulse. To get a worst-case estimate of phase error using this argument it will be necessary to estimate the surface velocity normal to the object surface as an acoustic wave propagates across it. For the sake of simplicity, assume that the normal (z) displacement, w(x,t) of the object surface resulting from a surface wave propagating in the x-direction may be described as a sinusoid as follows:

$$w(x,t)=\frac{w_0}{2}+w_0 sin(\omega t-k_a x),$$

where k_a is the acoustic wave propagation constant $2\pi/\lambda_a$ and ω is the acoustic frequency. The displacement velocity, then is:

$$\frac{dw}{dt}=w_0 cos(\omega t-k_a x),$$

the maximum of which will occur when $(\omega t-k_a x)=0$. Thus

$$\frac{dw}{dt}\Big|_{max}=w_0\omega.$$

An acoustic frequency of 500kHz corresponds to an acoustic wavelength of about

6mm for aluminum where the surface wave velocity is 92% of the bulk shear wave velocity. In the experiments documented here, a frequency doubled Nd:YAG laser (λ=532nm) with a half amplitude pulse duration of 9ns is used. Therefore the phase uncertainty, $\Delta\phi$, associated with the finite recording pulse width is

$$\begin{aligned}\Delta\phi &= 2k(w_0\omega)T \qquad (27)\\ &= 2\frac{2\pi}{532\times10^{-9}}(2\pi 500\times10^{3})(9\times10^{-9})w_0\\ &= 6.68\times10^{5}w_0 \textit{ radians}\\ &= 3.83\times10^{7}w_0 \textit{ degrees.}\end{aligned}$$

Thus for a peak wave amplitude $w_0=\frac{\lambda}{2}$ or 266nm, the phase uncertainty $\Delta\phi$=1°. Bear in mind that a surface displacement as large as 266nm will produce one holographic fringe in the interference field. Consequently a 1° phase error would still permit measurement of the wave peak to one part in 360 or about 0.3%. According to Equation 27, one may expect better base accuracy for smaller surface displacements.

Experimental Design

Three primary experiments were performed to demonstrate that heterodyne analysis of pulsed holograms can be used to measure sub-fringe displacements associated with traveling surface acoustic waves. In the first experiment, a CW heterodyne system designed very much after Dandliker's was built. Using this system, the processing electronics were optimized and sub-fringe interpolation to 1/900 of a fringe (2.9Å) was demonstrated. The last two experiments addressed the problems of synchronization of the laser output with the sound wave source for multiple exposure holography. As part of the third and final experiment, holograms recorded using the frequency doubled Nd:YAG laser were analyzd using heterodyne readout and phase detection.

CW Heterodyne Holographic Interferometry

The holographic recording system diagramed in Figure 14 was used to record a double exposure, dual reference beam hologram of the articulating surfaces of the tibial component of an artificial knee joint (see Figure 15). The two articulating

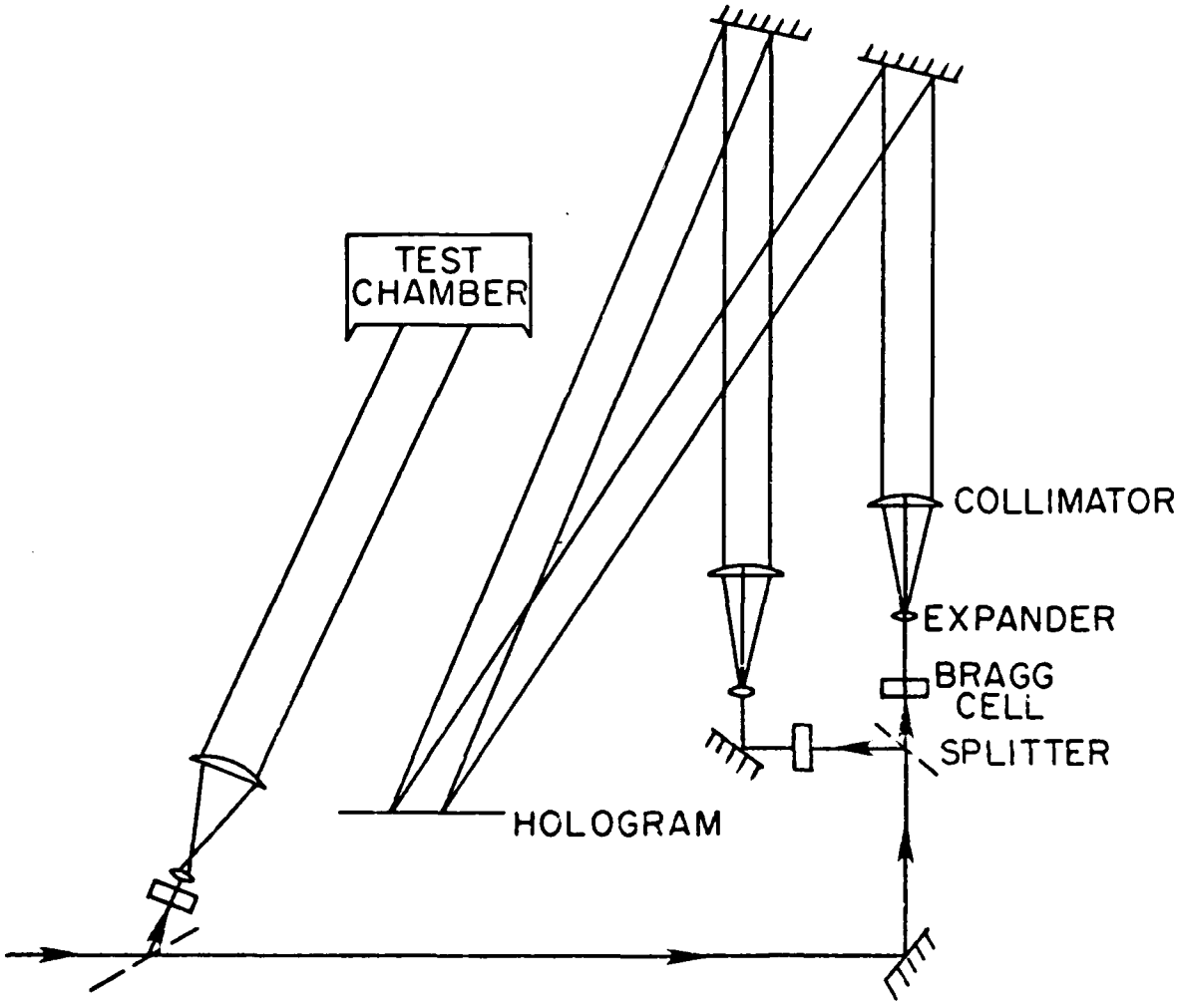

Figure 14: CW recording set-up for heterodyne holography.

surfaces are concave and serve as sockets into which the condyles of the upper, femoral, component are located. The object was placed in a sealed chamber such that the surfaces of interest could be viewed through the optically flat front window (see Figure 16). A contour hologram of the object was recorded using the multiple refractive index technique referenced earlier. By changing the pressure within the test chamber between exposures, the contour interval could be continuously adjusted so that less then one contour fringe could be observed over the image. Thus the details of the surface contour were revealed only by sub-fringe interpolation.

When recording a hologram, the beam from a Spectra-Physics 165 argon ion laser was split and directed through three acousto-optic modulators (refer to Figure 14). Each modulator (Isomet 1205C) was driven by an 80MHz signal from a single oscillator/driver during exposure. Beam ratios were adjusted so that either reference beam was one to two times as bright as the object beam at the film plane. A different reference beam was blocked for each exposure. Agfa 10E56-NAH film in a 4"x5" glass plate format was used. Total exposure was approximately 10 ergs/cm ^{2}. The film was developed for 5 minutes at room temperature using Kodak D-19 developer. After a 30 second rinse, the plate was fixed with Kodak rapid fixer for 5 minutes.

Once dry, the film plate was replaced in its holder for reconstruction and analysis. The beamsplitter used to provide illumination of the object was removed as was the etalon within the laser cavity. Both these steps increased the amount of light available in the reference beams. Precise replacement of the film plate was ac-

Figure 15: Artificial knee implant.

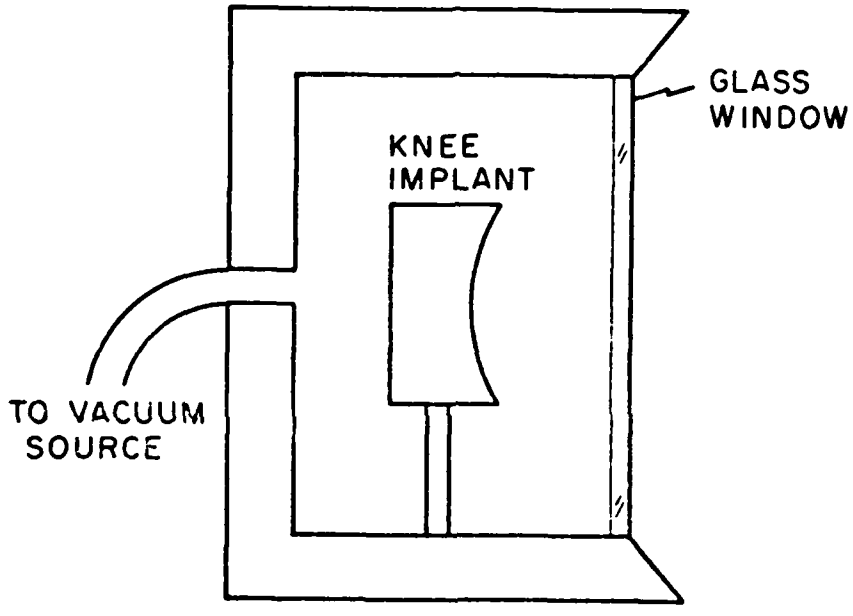

Figure 16: Test chamber for contouring knee implant.

complished by observing the interference pattern in the film plane and adjusting the film position and final reference mirrors to minimize the fringe order. Once the film plate was repositioned, the drive signal from one of the acousto-optic modulators was changed from the common 80MHz oscillator to a second oscillator this time running at 80.1MHz. Merit model R1500 silicon PIN diodes with integral transconductance amplifiers were used for signal detection. The reference detector was positioned for best S/N ratio. A second detector was mounted on an x-y translation stage driven by Newport Research model 850-1 linear actuators. The reference and probe signals were amplified by Tektronix AM501 differential amplifiers, passively band-pass filtered at 100kHz and fed to the reference and signal inputs of a PAR model 5301 lock-in amplifier. The lock-in amp was configured to measure phase difference between the reference and probe signals. The analog phase output signal was connected to the Y-axis input of a Hewlett-Packard 7045A x-y recorder. The x-axis was driven with a ramp signal from an HP 3304 function generator. (*In subsequent experiments probe detector positioning, phase voltage recording, processing, and display were all performed under computer control. The implementation of this computerized data acquisition and analysis system will be discussed later.*) Using the actuator joystick controller, the probe detector was positioned to one side of the output image and then scanned across the image at a constant velocity. The beginning of the probe scan was synchronized with the recorders x-axis drive signal. By incrementing both the recorder pen and the detector probe along the y-axis, a y-modulated raster scan of the knee prosthesis was generated.

Double Pulsed, Single Reference Beam Holography

A Quantel model 580-C Nd:YAG laser with an etalon and frequency doubling crystal was used to record all of the pulsed holograms. The laser has a horizontally polarized output with a pulse width of 9ns and an output energy of 1.2 joules/pulse at 1064nm and about half that energy at 532nm. The laser energy in the green (532nm) can be reduced either by intentional misalignment of the doubling crystal or by disabling the amplifier flash lamps. In the later case, the maximum energy per pulse at 532nm from the oscillator alone is 350mJ. It was this low evergy configuration which was used to record holograms of specularly reflecting objects. Recording of diffuse object surfaces required higher illumination intensities.

The recording geometry diagramed in Figure 17 was used to record the traveling surface wavefront propagating across an aluminum plate. The plate dimensions were 25cm x 38cm x 3.8cm thick. The front surface of the plate was grit blasted to provide a diffusely reflecting surface. The glass plate beamsplitter was positioned near the brewster angle to permit most of the beam energy to pass through it to illuminate the object.

The purpose of this experiment was in part to verify the timing and allignment of the pulsed holographic recording system. Since no fringe interpolation was to be done at this stage it was necessary that the recorded acoustic wavefronts be

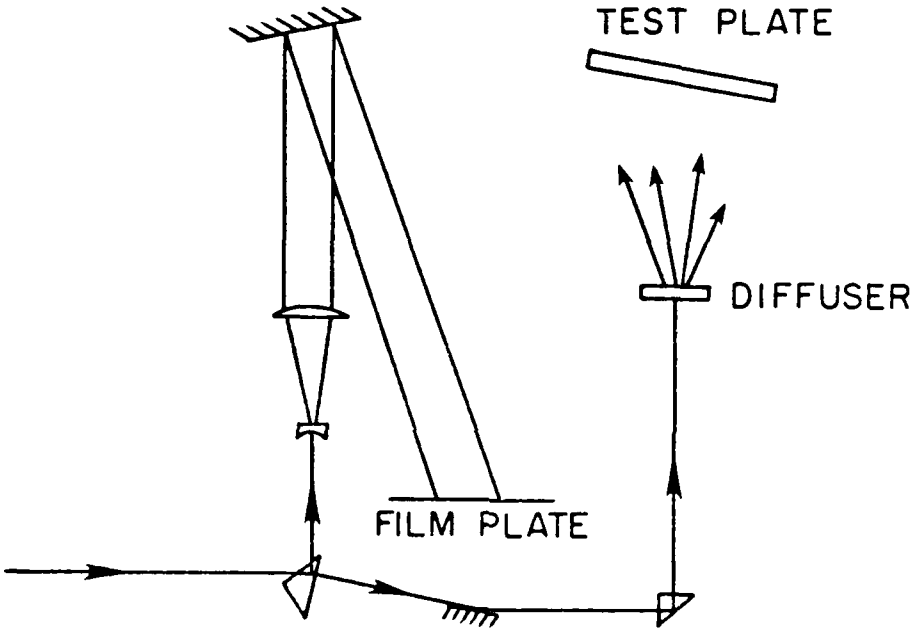

Figure 17: Double pulse holographic recording geometry.

sufficiently large to produce interference fringes which may be visually observed when the hologram is reconstructed. In order for this to occur the the surface wave displacement amplitude must be greater than $\lambda/2$ or about 2500A. To generate such large surface displacements a small explosive charge was used as the sound source. The explosive used was silver acetylide which is a white precipitate formed when acetylene gas is bubbled through an aqueous solution of silver nitrate. Once rinsed and dried, the silver acetylide powder was pressed into small pellets about 3mm in diameter and 0.5mm thick. Each pellet was then sandwiched between layers of cellophane tape and taped to the surface of the plate at the leftmost edge. The infrared output of the pulsed laser was focused on the pellet to detonate the explosion.

Assuming that the surface wave velocity is about 92% of the shear wave velocity in aluminum (3100 m/s), then the surface wavefront takes about 45μs to propagate half way across the plate surface. Since the same laser was used to detonate the explosion and record the hologram, it was necessary to modify the pockels cell triggering circuit to double pulse the laser during a single flash lamp pulse with a 45μs pulse separation. The pockels cell trigger circuit (Figure 18) uses eleven transistors in series which operate in avalanche mode to deliver a high voltage from capacitor C_1 to the pockels cell. Once avalanche is initiated the voltage across the series transistors must fall well below the avalanche threshold voltage before they will again turn off. It is the time required for this voltage decay which limits the rate at which the pockels cell may be triggered. To decrease the time required to reset the series transistors, an additional transistor was inserted across the pockels cell output terminals. This transistor turns on shortly after the high

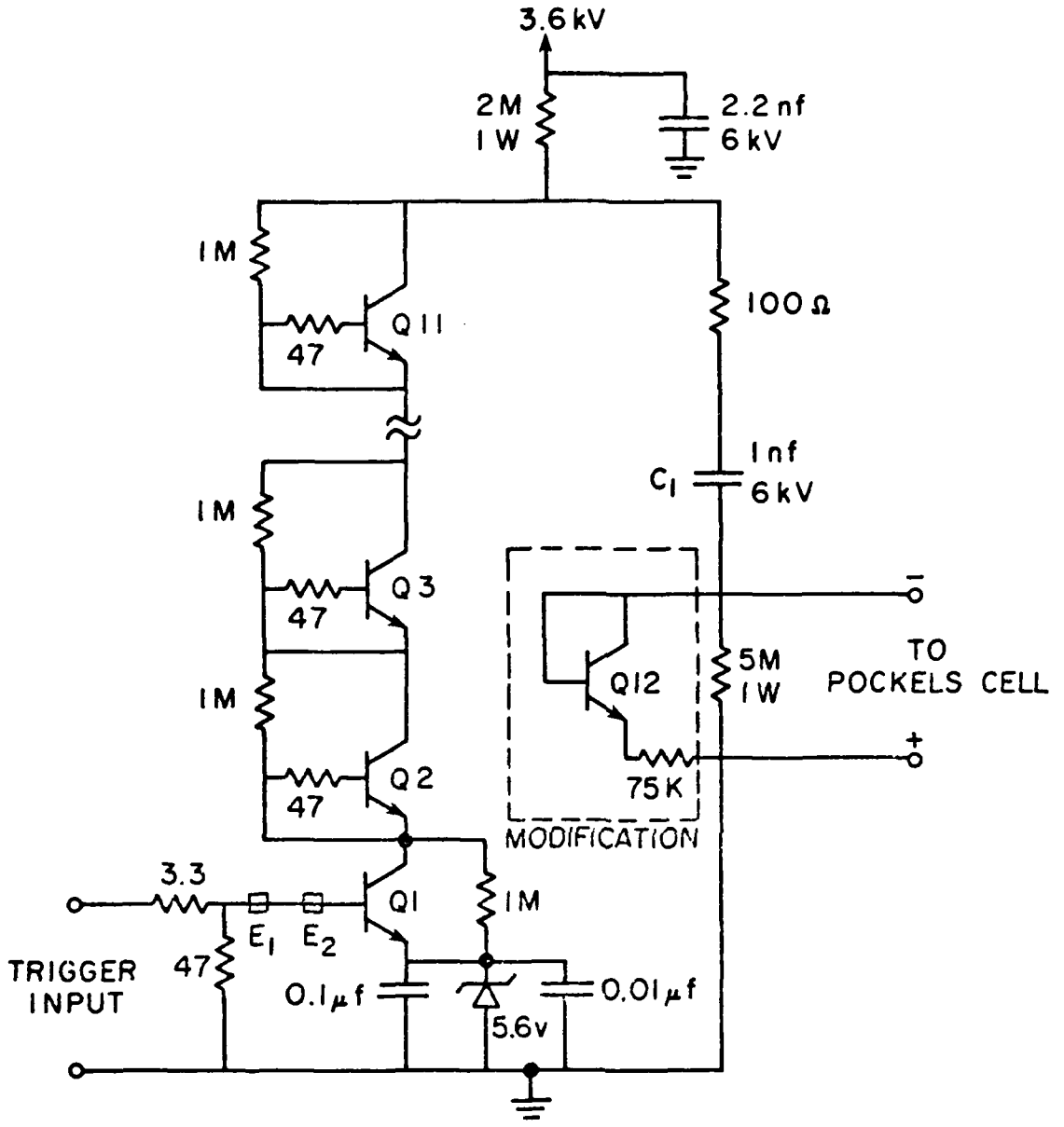

ALL TRANSISTORS: 2N5551

E_1, E_2 : FERROXCUBE 5659065-4A6

Figure 18: Q-switch trigger circuit.

voltage is applied to the cell. Once on, it provides a low resistance path which more rapidly bleeds charge from the capacitor thus causing a corresponding increase in the voltage decay rate. Once implemented, this modification permits double pulsing of the laser with pulse separations externally controlled over a range from 20μs to 100μs.

Optimum double pulsing of the laser required proper timing of the Q-switch pulses relative to the beginning of the flashlamp pulse. For this reason, the trigger system shown in Figure 19 was used. An adjustable digital delay generator (BNC model 7010) was used to trigger an HP model 8005B pulse generator with double pulse output. The delay unit was triggered by the flashlamp drive signal generated internally by the laser control electronics. A simple buffer circuit capable of providing the required 15 volt Q-switch trigger pulses into the 50 ohm trigger input circuit was designed and built since the TTL output of the HP pulse generator was insufficient to trigger the Q-switch.

The sequence for recording the pulsed acoustic surface wavefront was relatively straight forward. The pulse separation was set for 45μs and the digital delay adjusted to provide equal intensities in both pulses. The explosive charge was fixed to the plate surface and a film plate placed in the holder. When the laser was fired, a holographic exposure of the plate surface was recorded using the green line of the laser output. At the same time, the light from the infrared port of the laser detonated the explosive charge. Forty-five microseconds later, the laser emitted a second pulse of light. This time a second exposure of the hologram was made using the green wavelength so that any surface deformations caused by the explosion

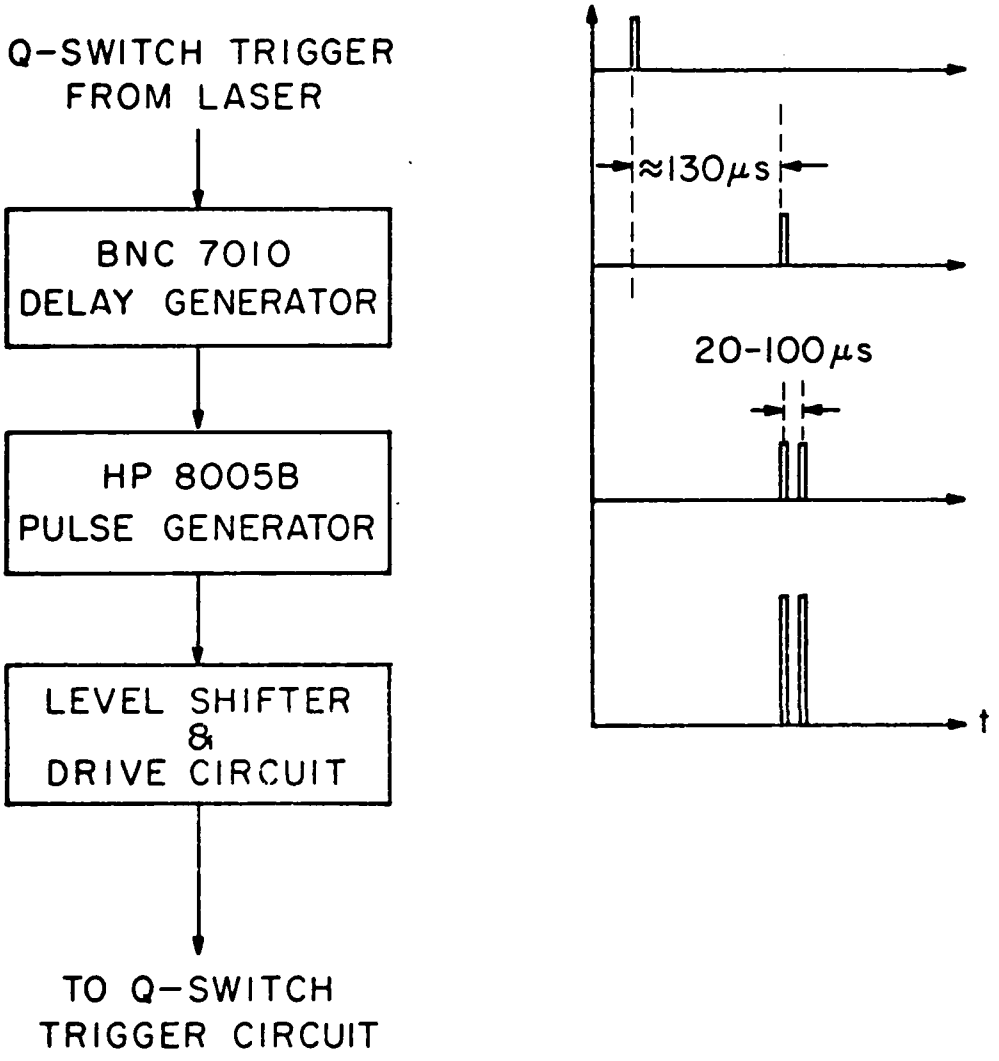

Figure 19: Laser trigger system and timing.

were recorded. The infrared beam again struck the plate. However, it was of no consequence since this time there was no charge to be detonated. Again Agfa 10E56 film was used for recording. Kodak D-19 developer for 5 minutes was followed by a water rinse. Instead of fixing these plates, however, the plates were beached for about 2 minutes in a solution of potassium dichromate and sulfuric acid to improve diffraction efficiency.

Surface Acoustic Wavefront Recording for Heterodyne Analysis

Through this experiment, the attempt to measure and display subfringe detail of displacements associated with surface wave propagation was made. The optical arrangement diagrammed in Figure 20 was used to record dual reference holograms of the surface wavefront generated by detonation of a silver acetylide pellet as described in the previous experiment. The same aluminum specimen used in the previous experiment was again used as the test object. This time however, the object surface was polished to reduce scattering of the collimated illuminating beam.

To facilitate heterodyne analysis, a dual reference beam double exposure hologram could have been recorded as described previously in the Background section. Using a double-pulsed laser to both detonate the expolsive charge and expose the

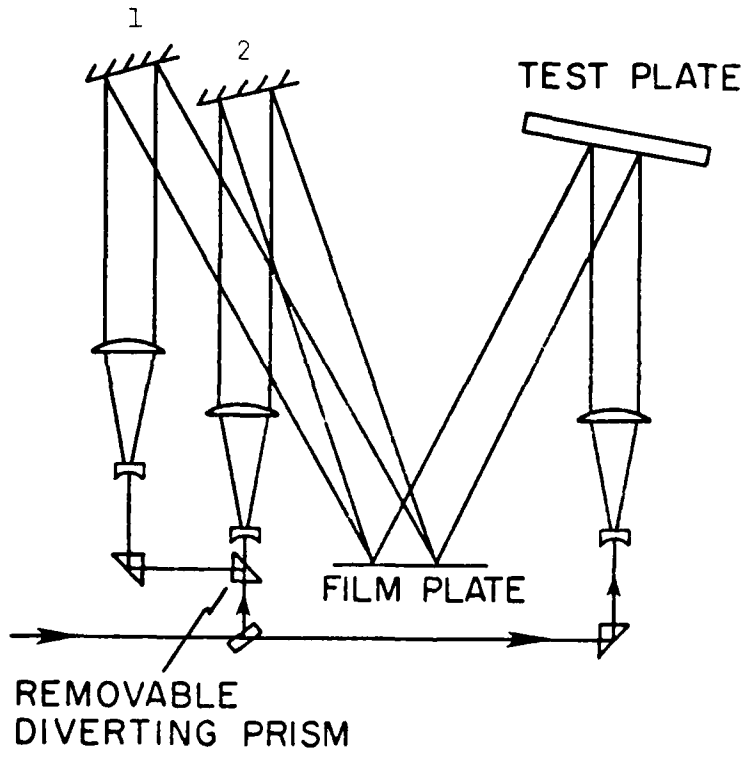

Figure 20: Triple exposure recording geometry.

holograms, however, would have required some type of electro-optic switch to change the reference beam path during the 45μs delay between the laser pulses. Unfortunately, such a switching device was not available for this experiment. Instead, a dual reference beam, triple exposure hologram was recorded. The first exposure was made using reference path 1 as shown in Figure 20. During this first exposure, the IR port of the laser was closed to prevent detonation of the explosive charge. After the diverting prism was removed, the IR port was again opened and the laser was double-pulsed to record exposures 2 and 3 using reference path 2.

While the triple exposure technique permits heterodyne analysis of the holographic interferogram, it has a pronounced effect on the calibration and sensitivity of the analysis. This effect can be understood by examining the mathematical description of the output of the triple exposure dual reference hologram. The intensity distribution in the output plane of the interferometer is nearly identical to that described by Equation 17 except that an additional image field, $\underline{O}_3$, must also be added in. Thus the intensity in the output plane becomes

$$
\begin{aligned}
I &= |o_1 e^{j(\omega_1 t+\phi_1(x,y))}+o_2 e^{j(\omega_2 t+\phi_1(x,y))}+o_3 e^{j(\omega_2 t+\phi_2(x,y))}|^2 \\
&= o_1^2+o_2^2+o_3^2+o_1o_2e^{j(\omega_1-\omega_2)t}+o_1o_3e^{j[(\omega_1-\omega_2)t+\phi_1-\phi_2]} \\
&\quad +o_1o_2e^{-j(\omega_1-\omega_2)t}+o_2o_3e^{j(\phi_1-\phi_2)}+o_1o_3e^{j[(\omega_1-\omega_2)t+\phi_1-\phi_2]}+o_2o_3e^{-j(\phi_1-\phi_2)} \\
&= o_1^2+o_2^2+o_3^2+2o_2o_3\cos(\phi_1-\phi_2)+2o_1o_2\cos(\omega_1-\omega_2)t+2o_1o_3\cos[(\omega_1-\omega_2)t+(\phi_1-\phi_2)] \\
&= o_1^2+2o_2^2+2o_3^2\cos\Delta\phi+(4o_1o_2\cos\frac{\Delta\phi}{2})\cos(\Delta\omega t+\frac{\Delta\phi}{2})
\end{aligned}
$$

for

$o_2 = o_3$

$\Delta\phi = \phi_1 - \phi_2$

$\Delta\omega = \omega_1 - \omega_2$

$$I = M\cos(\Delta\omega t + \frac{\Delta\phi}{2})$$

where

$$M = \frac{4o_1o_2\cos\frac{\Delta\phi}{2}}{o_1^2 + 2o_2^2(1+\cos\Delta\phi)}.$$

It is clear from the final form of this expression that the measured phase differences using the triple exposure technique will be half that which would be measured using the double exposure technique. Further, the modulation index will be zero when $\Delta\phi$ has a value equal to odd multiples of 180° and will be negative for $180° < \Delta\phi < 540°$ the effect of this negative modulation index is to generate a 180° discontinuity in the output of the phase detector when the optical phase difference between corresponding points on o_1 and o_2 exceeds 180°. Fortunately, for subfringe displacements, optical phase differences will always lie between +180° and -180° thus insuring that the modulation index will always be positive. As the modulation index falls below 1, the signal to noise ratio degrades as described earlier. Again for small displacements, this may not be a real problem since M will always be between 0.8 and 1.0 for optical phase differences between 0° and ±120°.

Taking the above into consideration it was felt that the triple exposure technique could be used to demonstrate the application of heterodyne analysis to

pulsed holographic interferometry. The triple exposure hologram was recorded on Agfa 10E56NAH plates and processed as before. The processed plates were then placed in the heterodyne readout system diagrammed in Figure 21. The plates were reversed in the film holder so that the conjugate, real image was projected on the output plane without requiring imaging lenses. Alignment was performed with both A-O modulators driven at 80.0MHz so that a stationary fringe pattern could be observed. Once the system was aligned, the modulators were driven at 80.0MHz and 80.1MHz, respectively.

Figure 22 shows the data collection system in block diagram form. Again, two Merit R1500 optical detectors were used to pick up the 100kHz beat signal. This time, however, no beamsplitter was used to provide a reference signal. Instead, the reference detector was placed in the output plane at one corner of the projected image. The scanning detector was mounted on an x-y translation stage driven by two NRC 850-C motorized micrometers. The micrometers were driven through an interface controlled by a Rockwell AIM 65 microcomputer. All micrometer drive routines were written using FORTH programming language and are listed in the Appendix. After selecting the appropriate vertical position with the y-axis micrometer, the horizontal scan routine was run. This routine scanned the photodetector over a distance of about 1cm in 125μm increments. After each increment, a trigger pulse was sent by the AIM 65 to the A/D converter module of an IBM model 7406-1 Device Coupler. The trigger pulse signaled the module to convert the analog phase difference signal from the lock-in amp and to transmit that digitized value through an RS232 interface to an IBM 5100 computer. The 5100 computer was used to decode the digitized data and store the data in vector form such

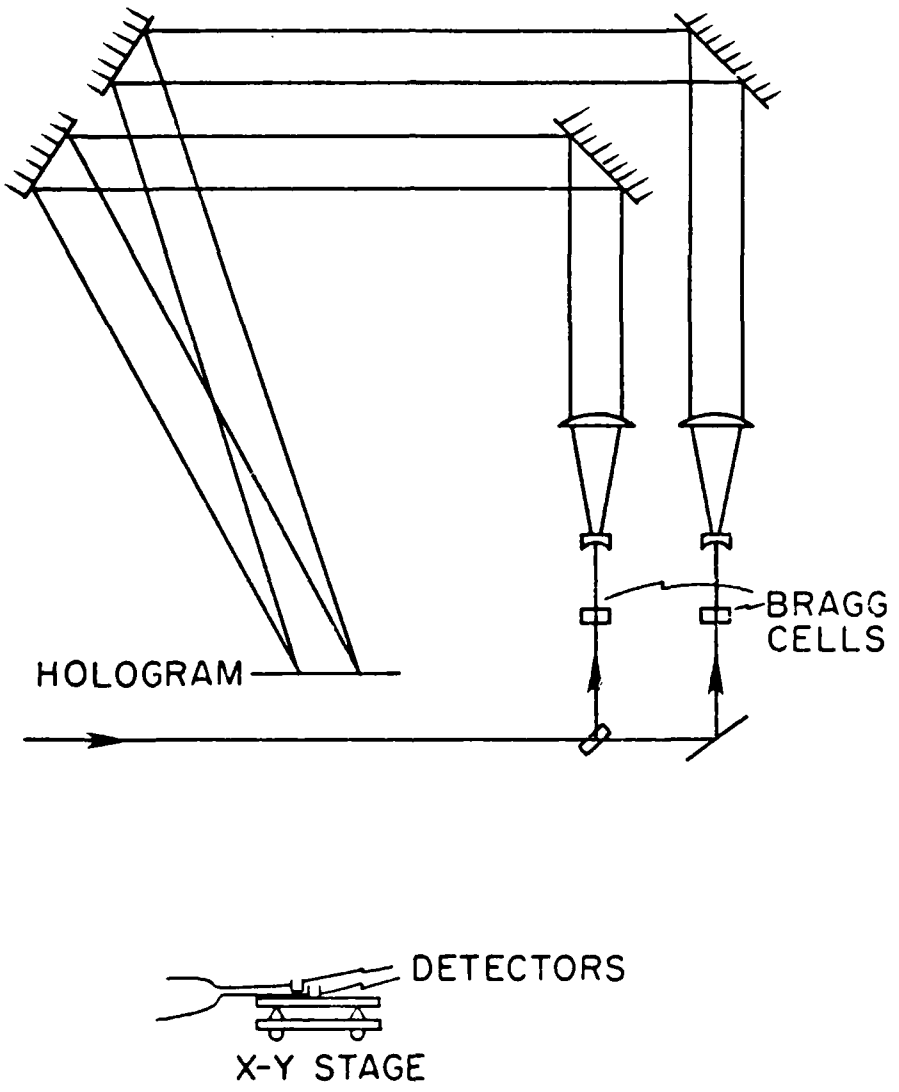

Figure 21: Readout geometry.

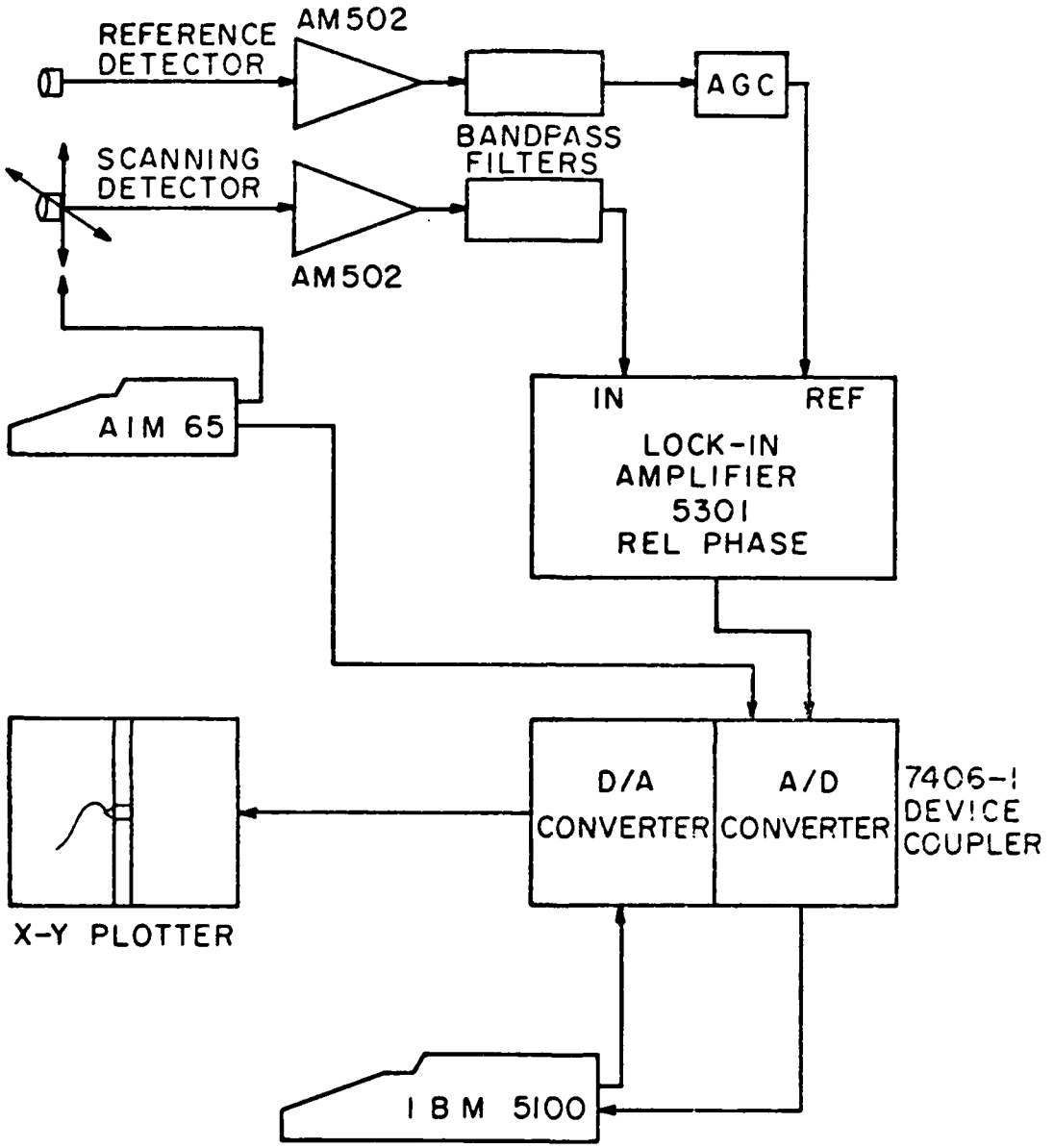

Figure 22: Readout, processing, and display system.

that each 90 element vector corresponded to one scan across the output field. The raw data received by the computer is modulo 360° in that phase values measured by the lock-in amp are restricted to those between -180° and +180°. Consequently, a computer routine was used to "unwrap" the raw data to remove these large discontinuities. As predicted with the relatively large surface displacements associated with an explosive sound source, 180° discontinuities in the data are also observed. These too are removed by computer processing. Finally the processed data was plotted on a Tektronix 4013 graphics display terminal and subsequently plotted on a Hewlett-Packard 7045A x-y recorder using the Analog Output Module of the Device Coupler. All collection and processing software in the IBM 5100 computer was written in APL and is listed in the Appendix.

Results and Discussion

Sub-fringe Interpolation: Contour Holography

The image shown in Figure 23 is the output of the dual reference contour hologram of the knee implant recorded as described in the previous chapter. In order to photographically record the contour fringes in the output field, both A-O cells in the reference legs were driven at the same 80.0MHz drive frequency. During heterodyne analysis, the two modulating frequencies differ by 100kHz thus causing the fringe pattern to fluctuate at such a high rate that the fringes are no longer visible. Optical detectors in the output plane, however, detect the sinusoidally varying intensity and transduce it into a voltage signal analog. Initially, the position of the scanning detector relative to the reference detector in the output plane was fixed and the phase difference as a function of time was plotted in order to measure system noise. Using this technique, the short term phase noise was characterized as having peak-to-peak fluctuations of 0.288°. Long term drift of about 0.04° per minute was also observed. In subsequent experiments, the drift rate was observed to deviate from this value indicating that drift may be in part the result of dimensional changes in the apparatus in response to changes in

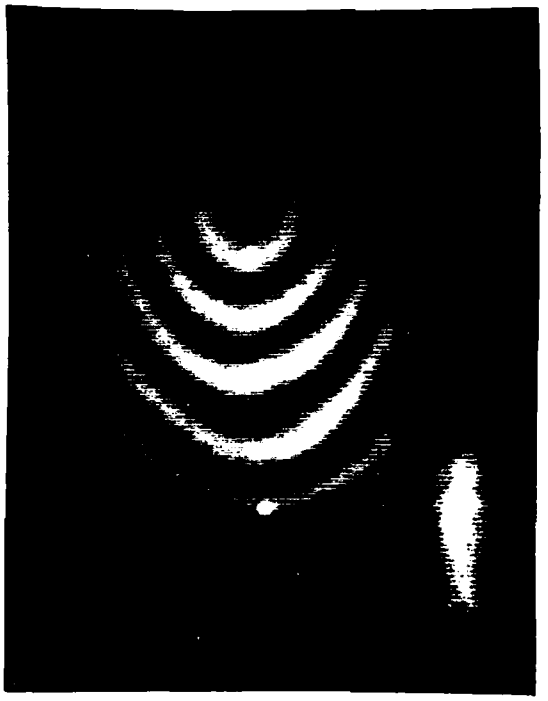

Figure 23: Output image fo Knee implant
when $\omega_1 = \omega_2 = 80$MHz.

environmental temperature.

The entrance pupil of the imaging optics was the film plate itself. Therefore the speckle size was determined by the 4 inch (10cm) dimension of the film plate. Given that the image plane was some 50cm behind the film plate, the speckle diameter was about 2.6 microns. The number of speckles, N, within the 1mm diameter detector was then about 1.5×10^{5}. From Equation 23, the expected phase error with $N=1.5\times10^{-5}$ and an estimated modulation index of 0.8 was about 0.11°. Therefore the overall phase noise may be as large as the sum of the elctronic and speckle noise or 0.4°. It should be noted that this 0.4° noise level corresponds to an optical path length sensitivity (for SNR = 1) of 0.57nm (5.7A) or an object displacement as small as 0.29nm (2.9A). In the specific case of contour holography, the sensitivity is 1/900 of the contour fringe interval.

A single horizontal line scan was made scanning from left to right across the image plane and passing through what would be the center of the stationary fringe pattern shown in Figure 23. Note that the plot of relative phase difference as a frunction of position is modulo 360° (Figure 24) and that if "unwrapped" it would provide a profile of the curved surface. However, sufficient sensitivity existed using this analysis system to detect the surface features of interest even when the holographic contour interval was larger than the depth of the surface relief over the entire object. Therefore, a second contour hologram was prepared using the double refractive index technique where, as described previously, only a slight change in air pressure inside the test chamber was made between exposures. The resulting contour image showed less than one complete fringe over the object.

AD-A155 405 HETERODYNE HOLOGRAPHIC INTERFEROMETRY FOR VISUALIZATION 2/2
OF SURFACE ACOUSTIC WAVES(U) JOHNS HOPKINS UNIV
BALTIMORE MD DEPT OF MATERIALS SCIENCE AND..
UNCLASSIFIED J W WAGNER NOV 84 ONR-85-1 N00014-82-K-0741 F/G 14/5 NL

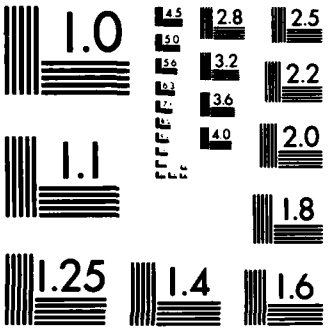

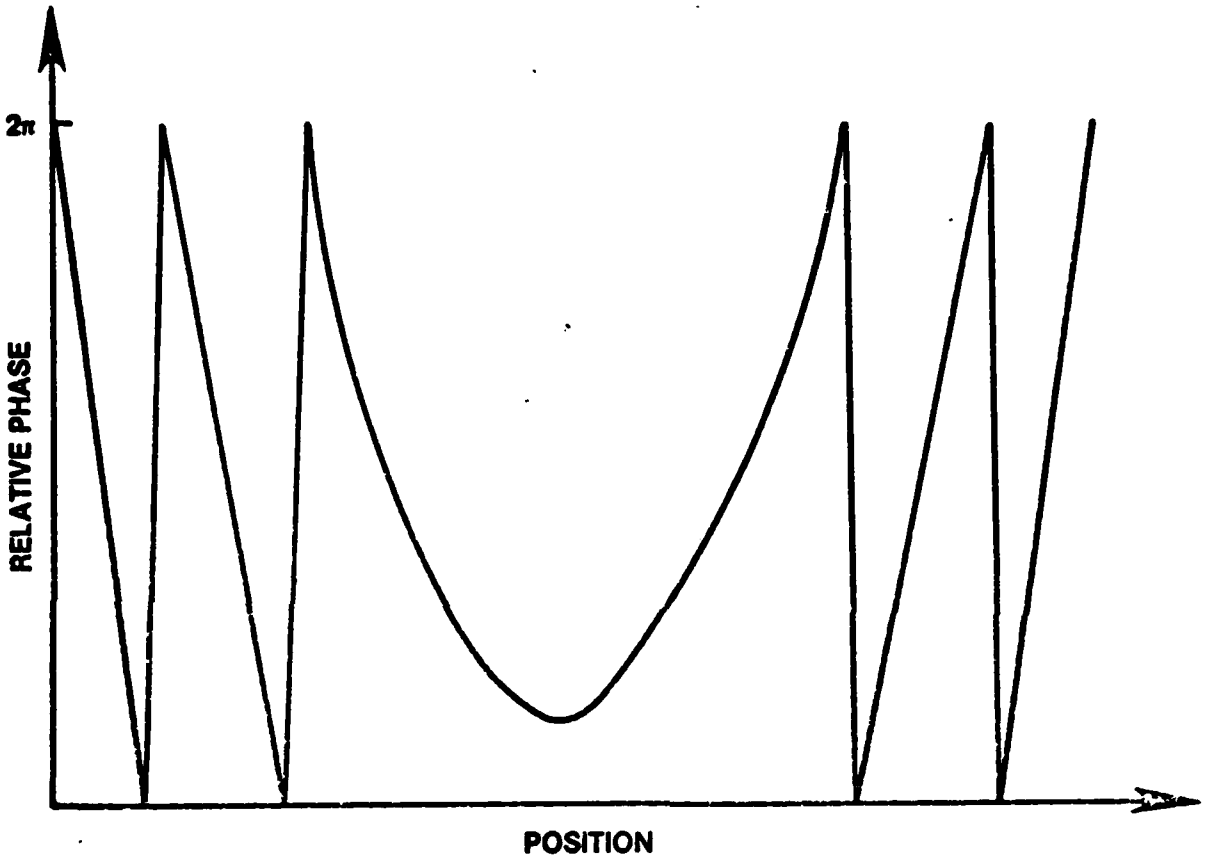

Figure 24: Single line scan across knee implant.

Thus when scanning over the image, the phase difference between the scanning and reference signals never exceeded 360°. Figure 25a shows a series of horizontal scans over a section of the image. The spacing between the scans corresponds to a vertical displacement of about 0.5mm along the image. The scans follow the normal curvature of the artificial knee socket. Just short of halfway across, all but the lowest scans show a deviation from the smooth contour. This deviation was caused by the gouge placed in the socket which was not apparent in the conventional contour hologram (Figure 23). A section of the gouge is shown in greater detail in Figure 25b by increasing the gain of the chart recorder. The displacement between scans is 0.1mm in this figure.

Double Pulsed, Single Reference Beam Holography

Photos of the reconstructed images of the aluminum plate recorded as described in the corresponding section of the previous chapter are shown in Figures 26 a, b, and c. Figure 26a shows the acoustic wavefront as it appeared 35 microseconds after the explosive charge was detonated. Figures 26b and 26c similarly show wavefronts from subsequent experiments where the laser pulse separation was 40 and 45 microseconds respectively.

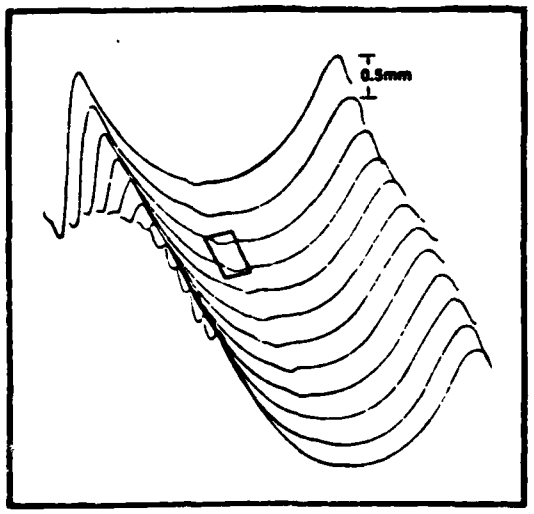

(a)

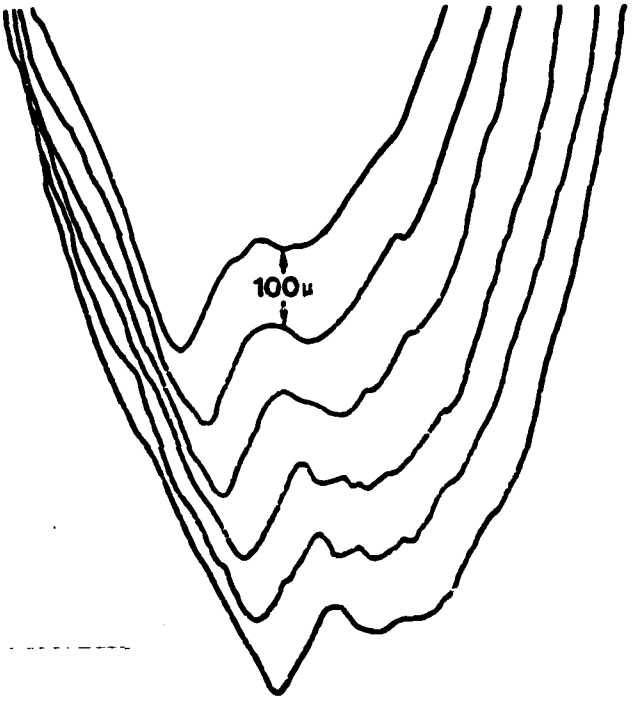

(b)

Figure 25: a) Full field scan of knee implant.
b) Enlargement of gouged region outlined in (a).

(a)

(b)

(c)

Figure 26: Double exposure holographic interferograms.
a) 35us b) 40us c) 45us.

From these photographs, the wave velocity and therfore the wave type can be determined. Table I summarizes the velocity data obtained from Figures 26 thus confirming that the observed primary wavefronts travel at a velocity corresponding to the Rayleigh wave velocity. Following the primary wavefront, one observes an irregular pattern of fringes. This pattern varies from experiment to experiment as the laser pulse interval is varied. Presumably this pattern is the result of surface displacements caused by the superposition of waves which are multiply reflected from the front and back surfaces of the test plate.

Heterodyne Analysis of Surface Acoustic Wavefronts

From the previous experiment it was confirmed that the primary surface wavefront passes across the center of the test plate some 45 microseconds after the explosive charge is detonated. This single data point was important since those holograms recorded for subsequent heterodyne analysis were made using the polished surface of the specimen as discussed earlier and only an 8cm diameter region was illuminated by the object beam. It was important, therefore, that the wavefront be passing through the 8cm circle when the final exposure of the hologram was made.

Two steps were involved in the alignment of the developed holograms in the heterodyne analysis system. Driving both A-O cells at the same frequency, a video

TABLE I

Pulse Separation	Distance Traveled	Velocity
35uS	45mm	2.66×10^5cm/sec
40uS	54mm	2.74×10^5cm/sec
45uS	59mm	2.61×10^5cm/sec

Expected Surface Wave Velocity = 92% x 3.1×10^5cm/sec = 2.85cm/sec

camera was focussed on the image plane. A cross which marked the center of the test surface was visible in the images reconstructed by both reference beams. Coarse alignment of the two images was obtained by changing the two reference beam angles to superimpose the two crosses observed on the video monitor. Final alignment was made by focussing the camera on the plane of the hologram plate and adjusting the reference beam angles to minimize the order of the observed fringe pattern. As predicted, the 10° separation of the reconstructing beams and the use of different recording and playback wavelengths made it impossible to eliminate all fringes observed in the hologram plane. Under the best alignment conditions, less than one fringe was observed over an area about 3cm in diameter in the center of the illuminated region. Beyond this central region, multiple fringes encircling the center were observed. Focussing back on the image plane, the effect of wavefront misalignment manifested itself in reduced fringe contrast and fringe distortion beyond the 3cm central region. Photographs of the output plane with proper and improper beam alignment are shown in Figure 27. Note the distortion of the fringes in Figure 27b resulting from slight misalignment.

Figure 28a shows relative phase difference as a function of position across a 1cm length of the image. This raw data is once again modulo 360° and exhibits the 180° discontinuities predicted for triple exposure heterodyne holography. Accounting for the discontinuities and "unwrapping" the data produces the plot of displacement versus position of Figure 28b. Two relatively narrow peaks are observed in the leading portion of this wavefront plot. Although it was beyond the scope of this research to explain these peaks, it was originally thought that they may be the result of the superposition of the surface wave emanating from the

a) Properly aligned

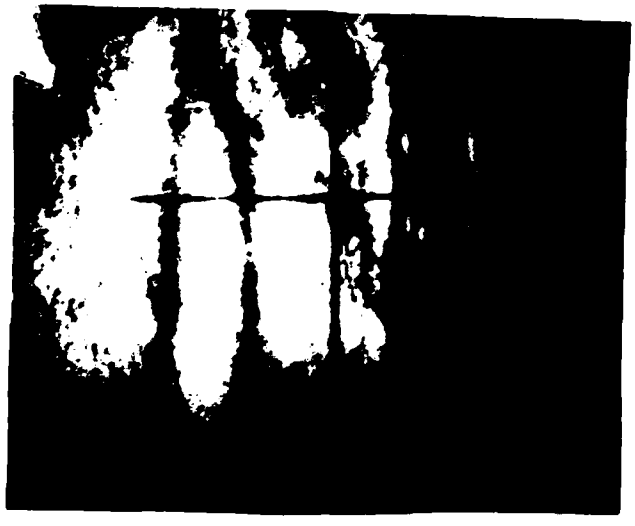

b) Improper alignment

Figure 27: Image plane recordings of dual reference beam holograms. Note curvature of fringes in improperlt aligned case.

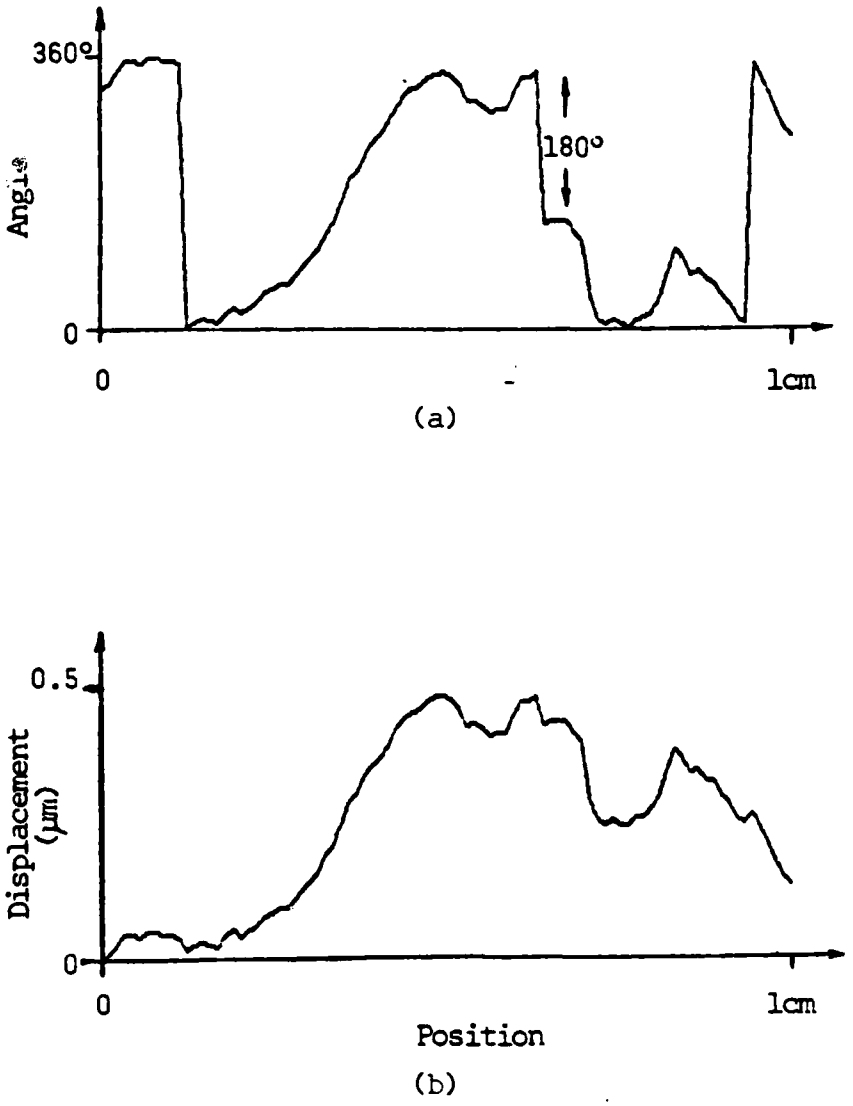

Figure 28: a)Phase difference data and b) corresponding displacement for a single 1cm scan across image.

source location with the wavefront which is reflected from the edge of the test plate immediately to the left of the charge. To test this hypothesis, a second experiment was performed identical with the first except that the charge location was displaced towards the center of the plate a full centimeter from the plate edge. Assuming that the twin peaks were the result of interference between the direct and reflected surface waves, the wave shape and especially the separation between the peaks should have changed. Instead, as can be seen from Figure 29, both the peaks and their relative spacing remained the same even after the charge location was changed. Therefore, edge reflection does not account for the dual peaks observed in the surface wave shapes. By changing vertical positions between scans, a full field raster over an area of the test surface can be obtained and plotted in "3-D" as shown in Figure 30.

Several sources of inaccuracy limited the resolution of this heterodyne analysis system. First, the measured efficiency of the triple exposure holograms was less than 1% providing an output field intensity of about 1 microwatt/cm ^{2}. From Equation 12, the expected phase variation was 0.06° for a fringe contrast of 0.7, a 1ms measurement interval, and a 10kHz bandwidth. In fact, the measured signal variation for a stationary scanning detector was 0.6° , which was much worse than predicted. The low signal intensity in the output plane and the relatively poor noise figure of the amplifiers used would tend to indicate that the detection system was not shot noise limited (a key assumption in deriving Equation 12). In addition some of the noise may be attributed to variation in pathlength owing to environmental effects.

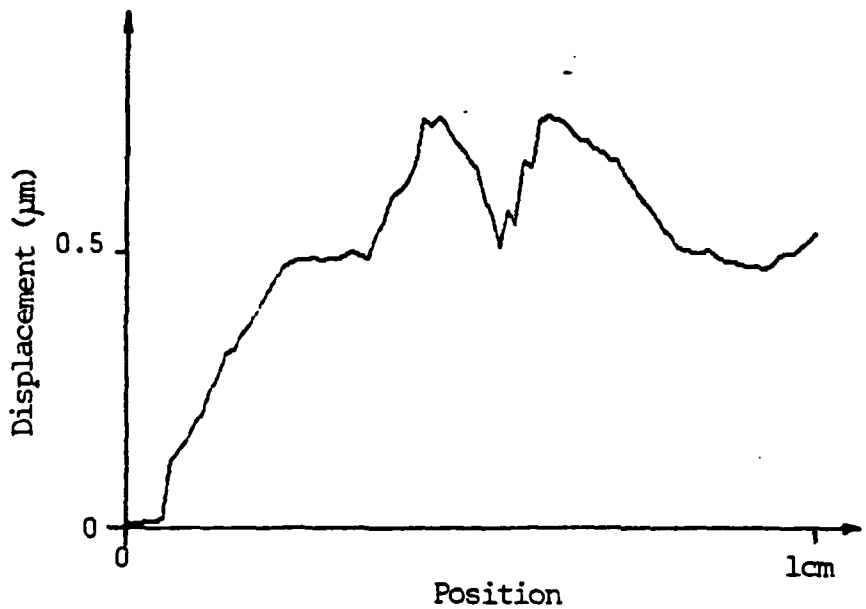

Figure 29: Displacement plot for a 1cm scan over the image recorded with the charge displaced by 1cm towards the center of the plate.

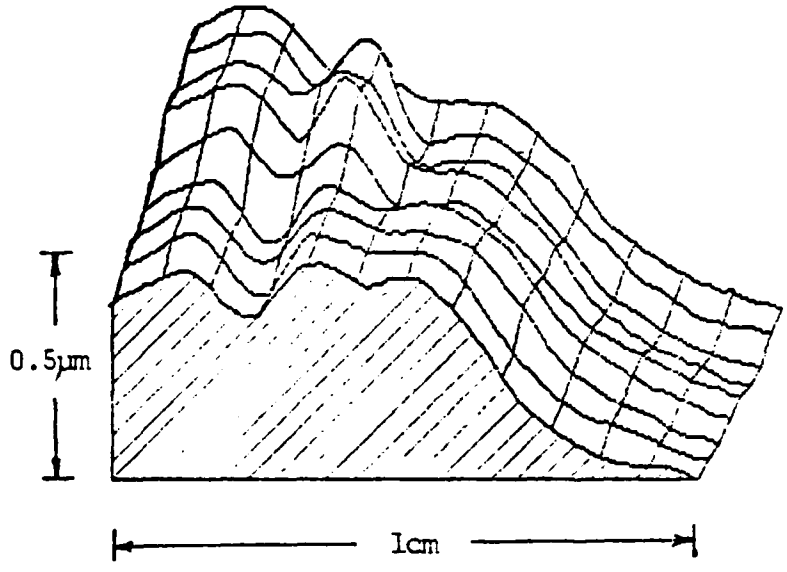

Figure 30: Multi-scan plot showing a portion of the surface wave displacement in "3-D".

A second noise source resulted from the effort to conserve light in the output plane by eliminating the need for focussing lenses. As a result, the distance, z, between the hologram and the output plane was a fairly long 61cm. The effective aperture of the imaging system was the 8cm diameter exposed region of the hologram. The speckle size was determined to be about 4.8 microns in diameter so that 4.4×10^4 speckles were encompassed by the 1mm diameter detector. Using Equation 23 the phase error resulting from speckle noise was on the order of 0.28°.

Finally, the rather large diameter of the detector itself caused some spatial averaging or smoothing of the surface features. As a result, one can not be certain of the absolute height of the leading edge peaks observed in Figures 31, 32, and 33. It is quite possible that these peaks are considerably larger than indicated.

Conclusions

Subfringe detail of traveling surface acoustic waves may be measured and displayed in full field using heterodyne holographic analysis of multiple exposure holograms recorded with a pulsed laser. Systems for recording and displaying surface wavefronts have been demonstrated to provide displacement resolution to 0.43nm (4.3A) over a 3cm diameter field. The limited field size is the result of using different recording and playback wavelengths. The field size may be improved to the size of the entire field recorded by the hologram by changing the recording and playback geometries to make the two reference beams more nearly colinear. Indeed when the same wavelength was used for both recording and analysis of the contour hologram, analysis of the entire field was possible.

The single most important step in improving the sensitivity of the heterodyne analysis system would be to increase the intensity of light in the output field. Several options are available to increase output intensity. First, holographic efficiency may be greatly improved by using a different recording medium either during the recording of the hologram itself or by copying the primary hologram onto a second medium using a longer CW copying process. Dichromated gelatins and photoresist holograms have been reported to have efficiencies over 90%. Using an electro-optic switch, as described earlier, to allow double rather than triple exposure holograms to be recorded for heterodyne analysis would not only improve holographic efficiency but would provide a constant fringe visibility in the output

plane independent of optical phase differences. Still more improvement could be expected if a higher frequency detector capable of sensitive recording at up to 80MHz were used. This would permit the use of only a single A-O cell for frequency shifting. Using the undiffracted beam for one reference, and the diffracted beam for the other reference, virtually all of the light from the laser would be projected on the hologram. Presently, the undiffracted beams from the two A-O modulators are blocked off and that energy is lost.

Increasing the light available in the output plane would also make it possible to further reduce spatial noise in the system. With more light available, a lens system may be used to reduce the working distance behind the hologram and thereby further decrease speckle size and thus improve phase accuracy. In addition, the detector area may be reduced to further improve lateral resolution as well.

The results of this work appear to support hypotheses proposed by the author and others working in the field of heterodyne holographic interferometry. Based on the experimental results obtained and the mathematical relationships which have been developed to describe system performance, the author feels confident in predicting that a practical system for studying sub-Angstrom transient phenomena may be realized using heterodyne holographic interferometry.

REFERENCES

F. Able, Applications of double exposure holographic interferometry to the investigation of early deformation of hard materials impacted by projectiles (French), Doctoral Dissertation, University of Besancon, 1976.

R. Adler, IEEE Spectrum May, 42-54 (1967).

C. Aleksoff, Applied Optics 10(6), 1329-1341 (1971).

L.K. Anderson and B.J. McMurtry, Applied Optics 5(10), 1573-1587 (1966).

R. Aprahamian, et al., Exp. Mech 11, 357 (1971).

W.P. Chu, D.M. Robinson, and J.H. Goad, Appl Optics 11, 1644 (1972).

R.J. Collier, C.B. Burckhardt, L.H. Lin, *Optical Holography*, (Academic Press, New York, 1971a), pp. 22-26.

R.J. Collier, C.B. Burckhardt, L.H. Lin, *Optical Holography*, (Academic Press, New York, 1971b), pp. 311-336.

R. Dandliker, B. Ineichen, F. Mottier, Optics Comm 9(4), 412-416 (1973).

R. Dandliker, Progress in Optics 17, 1-84 (1980).

DeLaRue et al., Proc IEE 119(2), 117-126 (1972).

D.C. Emmony, M.W. Godfrey, and R.G. White, J. Acoust. Emission 1(4), 263-265 (1982).

R.M. Gagosz, in *Holographic Nondestructive Testing*, edited by R.M. Erf (Academic Press, New York, 1974), pp. 61-85.

J.W. Goodman, in *Laser Speckle and Related Phenomena*, edited by J.C. Dainty (Springer, Heidelberg, 1975), pp. 46-51.

J.W. Goodman, *Introduction to Fourier Optics*, McGraw-Hill Book Co., 1968.

S.C. Gustafson, Optical Engineering 19(6), 849-852 (1980).

S. Hard and O. Nilsson, Applied Optics 17(23), 3827-3836 (1978).

B. Ineichen, R. Dandliker, and J. Mastner, in *Applications of Holography and Optical Data Processing*, edited by E. Marom, A.A. Friesem, and E. Wiener-Avnear (Pergamon, Oxford, 1977), pp. 207-212.

A.R. Jacobson, Rev Sci Instrum 53(6), 918-919 (1982).

T.H. Kwaaitall, B.J. Luymes, and G.A. van der Pijl, J. Phys D: Applied Physics 13, 1005-1015 (1980).

B.P. Lathi, in *Random Signals and Communication Theory*, (International Textbook Co., Scranton, 1968), pp. 175-187.

D.C. Leiner and D.T. Moore, Rev. Sci Instrum 49(12), 1702-1705 (1978).

N.A. Massie, R.D. Nelson, and S. Holly, Applied Optics 18(11), (1979).

J. Mastner and V. Masek, Rev Sci Instrum 51(7), 926-931 (1980).

R.S. Mezrich, K.F. Etzold, and D.H.R. Vilkomerson RCA Review 35, 483-519 (1974).

D.B. Neumann, presented at the OSA Topical Meeting on Hologram Interferometry and Speckle Metrology at N. Falmouth, Cape Cod, Mass., 1980. (Technical Digest)

C.H. Palmer and R.E. Green, Jr., Appl. Optics 16, 2333 (1977).

C.H. Palmer and R.E. Green, Jr., in *Nondestructive Evaluation of Materials*, edited by J.J. Burke and V. Weiss (Plenum Press, New York, 1979), pp. 347-378.

E.R. Peck, S.W. Obetz, J Opt Soc Am 43, 505 (1953).

M.J. Rudd, Ultrasonic NDE using laser transducers, (1980).

G. Smeets, J. Acoust. Soc. Am 61(3), 872-875 (1977).

C.M. Vest, in *Holographic Interferometry*, (John Wiley & Sons, New York, 1979), pp. 67-104.

D. Vilkomerson, Appl Phys Lett 29, 183 (1976).

R.J. Wellman, *Laser Detection of Flaws in Solids*, U.S. Army, ERADCOM, Harry Diamond Laboratories Report #HDL-TR-1902, May 1980.

R. Whitman, L. Laub, and W. Bates, IEEE Trans Sonics - Ultrasonics 15, 186 (1968).

A. Yariv, in *Intro To Optical Electronics*, 2nd Edition, (Holt, Rinehart & Winston, New York, 1976), p. 297.

A. Yariv, in *Intro To Optical Electronics*, 2nd Edition, (Holt, Rinehart & Winston, New York, 1976), p. 281.

END

FILMED

7-85

DTIC